Simulation studies of hydrodynamic aspects of magneto-inertial fusion and high order adaptive algorithms for Maxwell equations

A Dissertation Presented

by

Lingling Wu

to

The Graduate School in Partial Fulfillment of the Requirements for the

Degree of

Doctor of Philosophy

in

Applied Mathematics and Statistics

Stony Brook University

August 2010

Stony Brook University

The Graduate School

Lingling Wu

We, the dissertation committee for the above candidate for the Doctor of Philosophy degree, hereby recommend acceptance of this dissertation.

Roman Samulyak
Associate Professor of Applied Mathematics and Statistics
Dissertation-Advisor

James Glimm
Professor of Applied Mathematics and Statistics
Chairman of Defense

Xiaolin Li
Professor of Applied Mathematics and Statistics
committee of Defense

Michael McGuigan
Scientist of Brookhaven National Lab
committee of Defense

This dissertation is accepted by the Graduate School.

Lawrence Martin
Dean of the Graduate School

Abstract of the Dissertation

Simulation studies of hydrodynamic aspects of magneto-inertial fusion and high order adaptive algorithms for Maxwell equations

by

Lingling Wu

Doctor of Philosophy

in

Applied Mathematics and Statistics

Stony Brook University

2010

Three-dimensional simulations of the formation and implosion of plasma liners for the Plasma Jet Induced Magneto Inertial Fusion (PJMIF) have been performed using multiscale simulation technique based on the FronTier code. In the PJMIF concept, a plasma liner, formed by merging of a large number of radial, highly supersonic plasma jets, implodes on the target in the form of two compact plasma toroids, and compresses it to conditions of the nuclear fusion ignition. The propagation of a single jet with Mach number 60 from the plasma gun to the merging point was studied using the FronTier code. The simulation result was used as input to the 3D jet merger problem. The merger of 144, 125, and 625 jets and the formation and heating of plasma liner by compression waves have been studied and compared with recent theoretical predictions. The main result of the study is the prediction of the average

Mach number reduction and the description of the liner structure and properties. We have also compared the effect of different merging radii.

Spherically symmetric simulations of the implosion of plasma liners and compression of plasma targets have also been performed using the method of front tracking. The cases of single deuterium and xenon liners and double layer deuterium - xenon liners compressing various deuterium-tritium targets have been investigated, optimized for maximum fusion energy gains, and compared with theoretical predictions and scaling laws of [P. Parks, On the efficacy of imploding plasma liners for magnetized fusion target compression, Phys. Plasmas **15**, 062506 (2008)]. In agreement with the theory, the fusion gain was significantly below unity for deuterium - tritium targets compressed by Mach 60 deuterium liners. In the most optimal setup for a given chamber size that contained a target with the initial radius of 20 cm compressed by 10 cm thick, Mach 60 xenon liner, the target ignition and fusion energy gain of 10 was achieved. Simulations also showed that composite deuterium - xenon liners reduce the energy gain due to lower target compression rates. The effect of heating of targets by alpha particles on the fusion energy gain has also been investigated. The study of the dependence of the ram pressure amplification on radial compressibility showed a good agreement with the theory. The study concludes that a liner with higher Mach number and lower adiabatic index gamma (the radio of specific heats) will generate higher ram pressure amplification and higher fusion energy gain.

We implemented a second order embedded boundary method for the Maxwell equations in geometrically complex domains. The numerical scheme is second order in both space and time. Comparing to the first order stair-step approximation of complex geometries within the FDTD method, this method can avoid spurious solution introduced by the stair step approximation. Unlike the finite element method and the FE-FD hybrid method, no triangulation is needed for this scheme. This method preserves the simplicity of the embedded boundary method and it is easy to implement. We will also propose a conservative (symplectic) fourth order scheme for uniform geometry boundary.

To my parents and Jinyu with all my love

Table of Contents

List of Figures

List of Tables

Acknowledgements

I would like to thank my advisor, Prof. Roman Samulyak, for the exciting topics suggested, for interesting discussions and for his guidance and continuous support. He opens windows for me to see the beautiful science world and keeps encouraging me.

I would also like to thank Prof. Glimm. He shared his valuable scientific experience and insights.

I am deeply indebted to Prof. Xiaolin Li for his guidance and sharing his wisdom on conducting scientific research.

It is an honor to have Prof.Michael McGuigan being on my dissertation committee.

I would like to thank all my groupmates and friends, especially Tianshi Lu, Shuqiang Wang, Xingtao Liu, Wurigen Bo and Hongren Wei. I always get more help than I expect whenever I knock their doors.

Chapter 1

Introduction

This Dissertation deals with two main problems: (i) numerical study of plasma jet driven magneto-inertial fusion (PJMIF) and (ii) numerical algorithms for Maxwell's equations in geometrically complex domains. Although these problems seem very distinct from the first point of view, they have common mathematical features requiring closely related numerical algorithms. Mathematically, both problems are described by systems of hyperbolic partial differential equation with discontinuous material properties along geometrically complex interfaces. An advanced numerical method of front tracking have been developed for such systems and implemented in the FronTier code. In this work, we enhanced the FronTier code with new physics modules and used it for the numerical study of PJMIF. The embedded boundary method has been recently combined with the method of front tracking for the description of free surface magnetohydrodynamic flows in the low magnetic Reynolds number approximation [21] and multi-component elliptic and parabolic problems and the Stefan problem describing phase transitions [27]. In this work, we extend the embedded boundary method for discretizing Maxwell's equations in geometrically complex domains.

The two problems have also natural physics connection. The plasma jet driven magneto-inertial fusion operates with matter in extreme thermodynamic states. This area of science is also called high energy density laboratory plasma. While the main processes studied in this work can be sufficiently accurately approximated by pure hydrodynamic equations, a better approximation would require solving the resistive system of magnetohydrodynamic (MHD) equations. The use of MHD equations is especially important for the study of target physics which is beyond the scope of this work (except spherically symmetric simulations of the idealized target the main goal of which is the validation of certain theories and the fusion gain scaling laws). However the standard MHD approximation also fails at certain conditions and one has to resort to more fundamental description of the matter and fields such as two-fluid MHD, kinetic equations etc. Particle techniques [11] play an important role in the description of both neutral plasmas and systems of charged particles in electromagnetic fields. Therefore the research on numerical algorithms for Maxwell's equations in geometrically complex domains can be considered as the first step in the development of a fully electromagnetic particle-in-cell code suitable for the description of numerous problems involving plasmas and charged particles. Such a code would be critical for the complete PJMIF simulation. The success of the PJMIF techniques ultimately depends on the existence of high performance plasma guns. Numerical simulations will play a critical role in the optimization of plasma guns. In order to capture all physics processes in plasma guns, numerical simulations must be based on the electromagnetic particle-in-cell method in complex geometries. Therefore the research on Maxwell equations in complex geometries can be considered as the first step that will lead to end-to-end simulation studies of PJMIF.

Complicated geometry problem is one of most important field in numerical simulation. There are two main branches in this field, front capturing method, including Level Set method and Volume of Fluid method, front tracking method, including our front tracking method based on tracking of interface and marker point method.

[23],[7], [8].

1.1 Front Tracking Method in *FronTier*

FronTier is a computational package for the direct numerical simulation of multiphase flows based on the method of front tracking developed at Stony Brook University in collaboration with LANL and BNL [5, 20]. An important and unique feature of this package is its robust ability to track dynamically moving fronts or material interfaces.

Front tracking is a hybrid Lagrangian - Eulerian method. FronTier represents interfaces as lower dimensional Lagrangian meshes moving through a volume filling Eulerian grid. FronTier can evolve and resolve topological changes of a large number of interfaces in 2D and 3D spaces. The dynamics of interfaces is described by the theory of the Riemann problem for systems of conservation laws which is the problem of finding self-similar solutions to the systems of conservation laws with discontinuity of initial conditions at one point. The main advantage of explicitly tracked interfaces is the absence (or large reduction) of numerical diffusion. Explicit geometrical interfaces also enable us to describe accurately physics processes occurring at material interfaces (for instance phase transitions).

1.1.1 System of Hydrodynamic Equations

The hydrodynamic equation system, which we call Euler equations, consists of conservation of mass equation, conservation of momentum equation and conservation of energy equation.

$$\frac{\partial U}{\partial t} + \frac{\partial F}{\partial X} = 0 \tag{1.1}$$

where

$$U = \begin{pmatrix} \rho \\ \rho u \\ E \end{pmatrix}$$

$$F(U) = \begin{pmatrix} \rho u \\ P + \rho u^2 \\ u(E + P) \end{pmatrix}$$

In order to close the system, an equation of state is required. And Energy is defined as

$$E = \rho e + \frac{1}{2}\rho * u^2 \tag{1.2}$$

MUSCL scheme (Monotone Upstream-centered Schemes for Conservation Laws) is used to solve the Euler equation with a five-point stencil $\{x_{i-2}, x_{i-1}, x_i, x_{i+1}, x_{i+2}\}$. MUSCL scheme is second order in space.

1.1.2 Front Tracking Method and its Implementation

Front Tracking method is implemented in *FronTier* library. The interface is explicitly tracked and Riemann problem is solved between two different components. In one-dimensional case, the interface is a point; In two-dimensional case, the interface is a bond with a start point and an end point information; In three-dimensional case, the interface is a mesh surface constructed by triangles.

For the same component, the N-dimensional Riemann problem will split into N directions. The one-dimensional MUSCL scheme is conducted. If the stencil is near the boundary or near an interface, the information of boundary condition or interface point will be adopted.

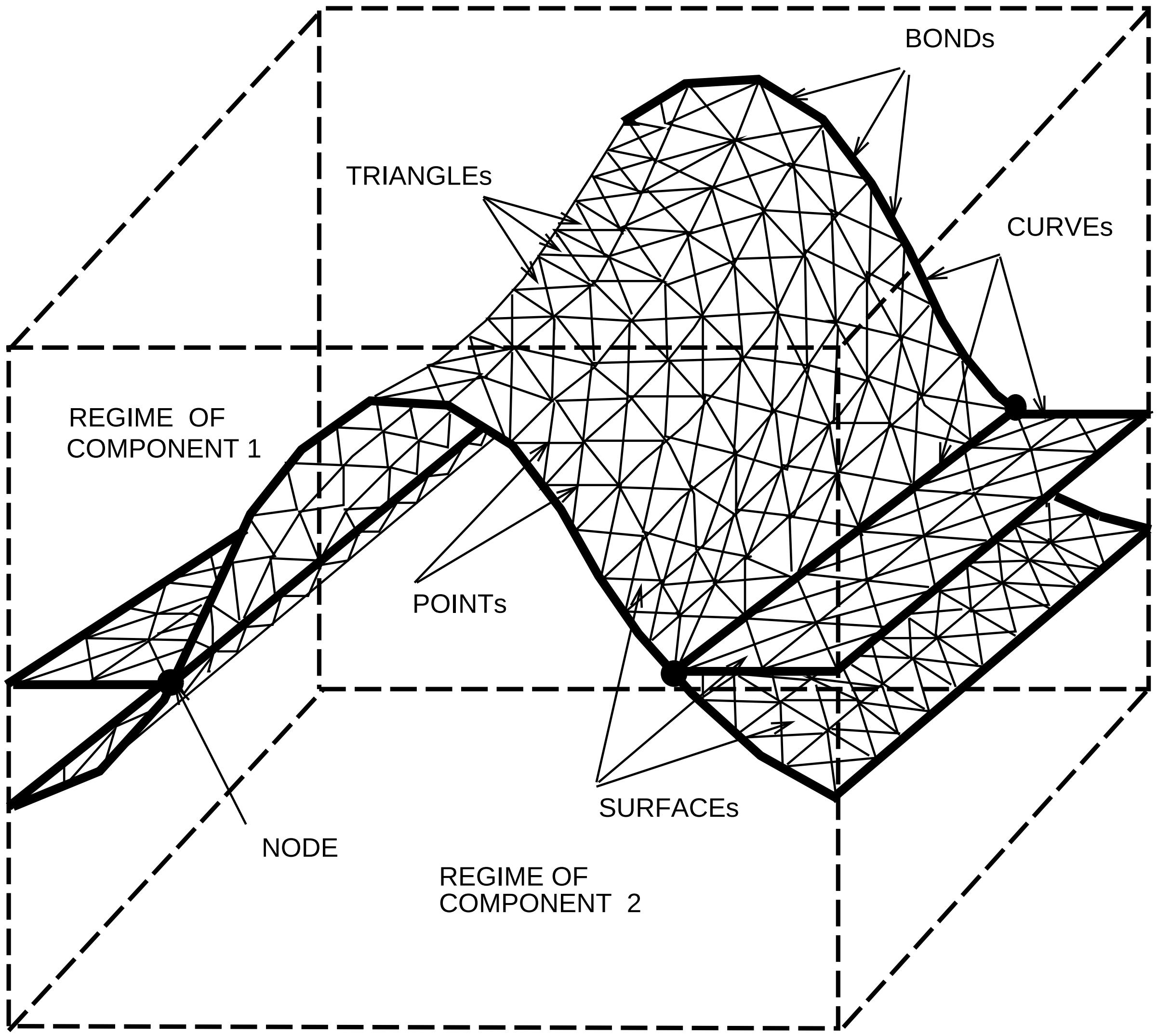

Figure 1.1: An illustration of the geometric data structures used for the front tracking method in three dimensions.

1.2 Embedded Boundary Method

The main idea of embedded boundary method is simple. It is a finite volume method. It extends the boundary cell or cut cell, which is smaller than a full cell, to a ghost full cell. The value of boundary cell will be represented by a constant value or some piecewise linear function or a high order function. The order of boundary cell approximation could be $n-1$, so the whole computational domain may have nth order if the interior part use nth order scheme.

1.2.1 Embedded Boudary Method in *FronTier*

Embedded boundary method is a conservative finite volume discretization for elliptic and parabolic equations [9], [16], [17]. Roman Samulyalk et al combined this method with front tracking method in the simulation of free surface flows at low magnetic Reynolds numbers [21]. Shuqiang Wang et al[27] extended this method to solve the elliptic and parabolic problem with interior boundaries or interfaces of discontinuities of material properties or solutions. Their code is implemented in *FronTier* and the second order accuracy is achieved in space and time. Unlike the immersed interface method, the embedded boundary method is conservative for fixed interior boundaries. For spatial discretization, They use linear interpolation to calculate the flux. For temporal discretization, they use two step implicit Runge-Kutta method. For interior cell, standard second order finite difference method or finite volume method is used. For partial cell containing two different components, two unknowns are defined for each component. One extra unknown is defined at the center of each partial cell interior boundary to facilitate the discretization of the jump conditions. A classical Stephan problem is solved to simulate the temperature increasing and melting of uranium fuel in the fuel assembly during the transient overpower and loss of coolant accidents.

1.2.2 Embedded Boundary Method for Maxwell equations

Maxwell equations:

$$\nabla \times E = -\frac{\partial B}{\partial t} \tag{1.3}$$

$$\nabla \times B = \mu_0 \epsilon \frac{\partial E}{\partial t} + \mu_c J \tag{1.4}$$

Here $E = (E_x, E_y, E_z)$, $E = (B_x, B_y, B_z)$, $D = \epsilon_0 E$, $B = \mu_0 H$.

Finite-difference time-domain (FDTD) [28] is a popular scheme for Maxwell equation. It is second order for regular grid and zero order for irregular grid, so if there exist some cut cells near the boundary, FDTD scheme will only show a first order accuracy.

For high order accuracy in complex geometry boundary, Supriyo Dey and Raj Mittra [4] introduced a technique for cut cells. The idea is following embedded boundary method. It is stable and second order.

1.3 Dissertation Organization

The rest of my thesis is organized as following: In Chapter 2 We present the one dimensional ideal symmetric liner target interaction results. In Chapter 3 two dimensional detached jet simulation results with flow through boundary condition. In Chapter 4 we explore the three dimensional liner structure. In Chapter 5, we review FDTD and the embedded boundary method for Maxwell equations.

Chapter 2

Spherical Symmetric Simulation of Plasma Liners Implosion and Target Compression

2.1 Introduction for PJMIF

Nuclear fusion is potentially an unlimited and environmentally clean source of energy. But practical realization of the nuclear fusion remains a challenging unsolved problem for several decades.

Two traditional approaches to nuclear fusion are the inertial confinement fusion (ICF) and the magnetic confinement fusion (MCF). The main advantage of the magnetized target inertial fusion approach compared to the conventional inertial confinement fusion, which has no embedded magnetic field, is the potential for reducing the driver power needed to achieve ignition conditions in the central hot spot [13] - [10]. In the magnetized target, the transport of heat and energetic fusion alpha particles is greatly reduced. The conventional magneto-inertial fusion method uses an imploding solid metal liner in cylindrical or spherical geometry to adiabatically compress a preformed magnetized plasma target [24]. The proposed targets are either spherical ones formed by two compact toroids of fusion materials containing magnetic fields in the force-free Woltjer-Wells-Taylor state of minimum energy, or linear targets, such as a Z-pinch [19].

A longstanding concern with most solid liner driven MIF concepts is the "stand-off problem": the target-related hardware has to be located at a sufficient stand-off distance from the fusion hot spot in order to be reusable. Another important concern is the solid liner manufacturing cost. To solve these problems, Thio *et al.* [26] suggested that a spherical array of supersonic plasma jets launched from the periphery of the implosion chamber could be used to create a spherically symmetric plasma liner to implode the central magnetized target. Such a plasma liner is assembled when the jets intersect and merge with each other at an intermediate radius r_m, as shown schematically in Figure (2.1). The plasma liner was intended to have dual purpose: to serve as an imploding driver compressing the target and to provide surrounding deuterium fuel clad.

Figure (2.1) shows the three steps to form liner and liner imploding process. Uniformly distributed guns in the chamber wall will generate plasma jets simultaneously. After moving for several meters long, these jets will touch each other and generate a compression wave. Then a liner with the turbulence will keep a high speed implosion until the liner affects the magnetized target. In this paper, we will use *FronTier* code to simulate the liner merged by plasma jets and analysis the liner property.

Plasma is called the fourth state of matter. In fact it is a gas with the ionized particles. Unlike gas, plasma have a high conductivity and number of charge carriers. Hence when there is a magnetic or electric field, we need to introduce Maxwell equations and heat transfer problem into fluid equation system. However during the jet moving and liner merging process, hydrodynamic equations are sufficiently accurate.

There are numerous papers investigating different numerical methods to simulate the three-dimensional plasma liner. Charles E. Knapp [14] used implicit smooth particle method to solve the ordinary differential equations and simulated the two-

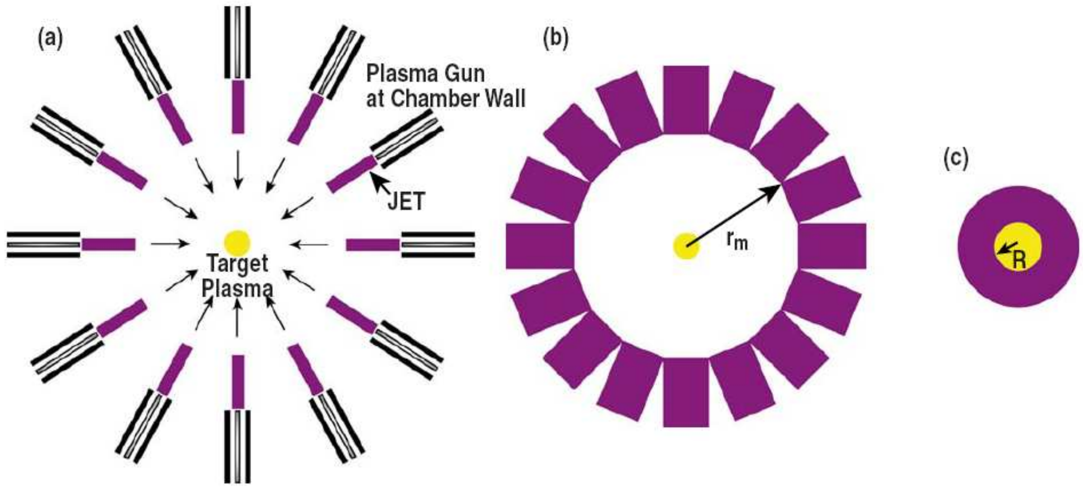

Figure 2.1: Schematic of the plasma jet induced magnetized target fusion. a) Plasma guns at the chamber wall shoot high velocity, supersonic plasma jets. b) Jets merge at the merging radius r_m and form a liner. c) Plasma liner implodes and compresses the target.

dimensional 2 jets merging and three-dimensional liner merging. He calculated 60 cylindrical D-T jets in a soccer ball pattern, but the distance from gun to target is only 20 cm which is not the same as the machine building now. Parks [18] analyzed a simplified model to calculate the energy ratio which we are also interested in. To compare with Parks' paper, We set a 6-meter numerical simulation first. Then we set two 3-meter numerical simulations to check what is the effect for the different merging radius.

A new experiment is being built now in Los Alamos National Laboratory [12]. This machine will merge 30 5-cm plasma jets with Mach number 10 to 35 and velocity 50 to 70 km/s in a 9 ft (2.74 meter) diameter spherical vacuum chamber. The goal is to reach high pressure (0.1 Mbar) via imploding plasma jets. The jets are injected and nearly fully ionized by HyperV coaxial plasma guns. HyperV claim that they recently achieved 100km/s. After merging, they could choose to use solid or gaseous target in the middle of the spherical chamber. The whole machine will be expected to run in Mar 2010 to Feb 2013.

For one dimensional ideal case, a symmetric liner and target simulation is performed. For three dimensional case, we decompose the whole computing process into two parts. First experiment will initialize the jet with uniform density, pressure and velocity. Then this detached jet will move 500cm in a high vacuum environment with Mach number 60 at the beginning. During this process, we solve the hyperbolic equation system by MUSCL scheme and track the status of the jet. The second step is to use the physical data from first numerical experiment to study the liner merging process. We initialize the total 144/125/625 jets by the result from the first detached jet experiment. These jets will penetrate each other and generate shock like compression wave, finally they will merge together to form a plasma liner. We will track the liner structure during this process by using MUSCL scheme.

2.2 Spherically symmetric simulation of PJMIF

The work in this section is published in [22].

2.2.1 Background and Motivation

Several simplified analytical and semi-analytical models have been used for the study of spherically symmetric PJMIF. The 1-D Lagrangian model [25] showed the target ignition and burn can be achieved in a target of a 1 mg plasma, 10 cm initial diameter imploded by a plasma liner with about 1 g of material, target magnetic field of 10 T, and implosion velocity of about 250 km/s. Without the magnetic field, the target temperature was limited to about 1 keV. Plasma jet induced PJMIF was also analyzed by Parks in [18] using a new theoretical model. [18] states that for a spherically imploding plasma liner shell with high initial Mach number, the rise in liner density with decreasing radius r goes as $1/r^2$, for any constant adiabatic index $\gamma = d\log p/(d\log\rho)$. The ram pressure of the liner is amplified on the target by the factor $A \sim C^2$, indicating strong coupling to its radial convergence $C = r_m/R$, where r_m is the jet merging radius, R is the compressed target radius, and A is the compressed target pressure divided by the initial liner ram pressure. The study showed that deuterium-tritium (DT) plasma liners with initial velocity of about 100 km/ s and $\gamma = 5/3$, need to be hypersonic $M \sim 60$ and thus cold in order to realize values of $A \sim 10^4$ necessary for target ignition. For optically thick DT liners, $T < 2$ eV, $n > 10^{19} - 10^{20}$ cm^3, black-body radiative cooling is appreciable and may counteract compressional heating during the later stages of the implosion. The fluid then behaves as if the adiabatic index were depressed below 5/3, which in turn means that the same amplification $A = 1.6 \times 10^4$ can be accomplished with a reduced initial Mach number $M \simeq 12.7(\gamma - 0.3)^{4.86}$, valid in the range of $10 < M < 60$. Analytical calculations indicated that the hydrodynamic efficiency for plasma liners assembled by current and anticipated plasma jets was less than 4%. The estimated confinement time was 100 ns. Finally, the study concluded that spark ignition of the DT liner fuel does not appear to be possible for magnetized fusion targets with typical threshold values of areal density $\rho R < 0.02$ g cm^2.

We have performed spherically symmetric simulations of the implosion of plasma liners and compression of plasma targets in the concept of the Plasma Jet driven Magneto Inertial Fusion (PJMIF) using the method of front tracking. The cases of single deuterium and xenon liners and double layer deuterium - xenon liners compressing various deuterium-tritium targets have been investigated, optimized for maximum fusion energy gains, and compared with theoretical predictions and scaling laws of [P. Parks, On the efficacy of imploding plasma liners for magnetized fusion target compression, Phys. Plasmas **15**, 062506 (2008)]. In agreement with the theory, the fusion gain was significantly below unity for deuterium - tritium targets compressed by Mach 60 deuterium liners. In the most optimal setup for a given chamber size that contained a target with the initial radius of 20 cm compressed by 10 cm thick, Mach 60 xenon liner, the target ignition and fusion energy gain of 10 was achieved. Simulations also showed that composite deuterium - xenon liners reduce the energy gain due to lower target compression rates. The effect of heating of targets by alpha particles on the fusion energy gain has also been investigated.

The main goal of this work is the verification of theoretical predictions and scaling laws of [18], gaining a better understanding of hydrodynamics of the PJMIF method, and finding ways of increasing the fusion energy gain via spherically symmetric simulations of the liner implosion and target compression. Although 1D simulations lack the accuracy of 3D studies with improved physics models and resolved spatial phenomena like fluid instabilities, they are an excellent tool for the quick exploration of new regimes and providing guidance to more refined simulations with resolved physics and spatial dimensions. While main conclusions of this work were obtained from 1D spherically symmetric simulations, full 3D simulations of the merger of jets and the formation and implosion of the plasma liner are in progress and will be reported in next chapters.

2.2.2 Main Equations

In this section, we perform detailed comparison of numerical simulations with theoretical predictions of [18]. The main formulas are summarized below.

The fusion energy gain was obtained in simulations using the following approach. At each time step, the production of fusion neutrons was calculated for each computational cell of the target based on the thermodynamic state of the target and the fusion reactivity [1]

$$< \sigma v >= c_1\theta(T)\sqrt{\frac{\left[BG^2/(4\theta(T))\right]^{1/3}}{D\,T^3}}\exp\left[-3\left[BG^3/(4\theta(T))\right]^{1/3}\right], \qquad (2.1)$$

where

$$\theta(T)=\frac{T}{1-\frac{T(c_2+T(c_4+Tc_6))}{1+T(c_3+T(c_5+Tc_7))}}.$$

Here the temperature T is in keV units, the dimension of the fusion reactivity is cm^3/s, and coefficients have the following numerical values $c_1 = 1.17302 \times 10^{-9}$, $c_2 = 0.0151361$, $c_3 = 0.0751886$, $c_4 = 0.00460643$, $c_5 = 0.0135$, $c_6 = -1.0675 \times 10^{-4}$, $c_7 = 1.366 \times 10^{-5}$, $BG = 34.3827$, $D = 1.124656 \times 10^6$. The neutron production was integrated in the target volume and time to obtain the total fusion energy

$$E_{\text{fusion}} = (e_{\text{neutron}} + e_\alpha)\int_{t_0}^{\infty}\int\int\int_{V_{target}(t)} < \sigma v > \frac{n^2}{4}\,dV\,dt, \qquad (2.2)$$

where n is the target number density, $e_{\text{neutron}} = 14.1$ MeV is the neutron energy and $e_\alpha = 3.5$ MeV is the alpha particle energy released in the process of fusion.

Finally, the fusion gain was obtained as

$$G_{\text{simulation}} = E_{\text{fusion}}/E_{\text{liner}}, \qquad (2.3)$$

where

$$E_{\text{liner}} = E_{\text{kinetic}} + E_{\text{internal}} \simeq E_{\text{kinetic}}$$

is the total initial energy of the liner. Notice that (2.3) does not account for the efficiency of electromagnetic plasma guns that generate plasma jets. The efficiency of the plasma guns is not precisely known. We believe that it is currently in the range of 20% - 70% and can be increased in the future as the technology develops.

We will compare the simulated fusion energy gain (2.3) with theoretical estimates of [18] obtained as follows. If all the deuterium - tritium fuel in the target could be burned up, then the maximum (ideal) fusion energy gain would be 293 at the ignition temperature of 10 keV. The actual fusion energy gain is

$$G_{\text{theory}} = 293 f_b \eta_h. \tag{2.4}$$

In this expression, η_h is the hydrodynamic efficiency and f_b is the fuel burn up fraction coefficient

$$f_b =< \sigma v > n\tau_{dc}/2, \tag{2.5}$$

where n is the target number density and τ_{dc} is the deconfinement time defined as the time during which the pressure in the target decreases by the factor of two compared to the fully compressed state. The hydrodynamic efficiency is defined as the ratio of the internal energy of the compressed target to the initial energy of the liner,

$$\eta_h = \frac{E_{\text{target}}}{E_{\text{liner}}}, \tag{2.6}$$

where

$$E_{\text{target}} = \frac{PV}{\gamma - 1}.$$

According to [18], the hydrodynamic efficiency can be expressed as

$$\eta_h = \frac{R}{L} H\left(\gamma, M_{\text{liner}}\right), \tag{2.7}$$

where R is the compressed target radius, L is the initial thickness of the liner (the length of merging jets), and H is a function of the adiabatic gamma and the initial Mach number of the liner. $H = 1.23$ for $\gamma = 5/3$ and $M_{\text{liner}} = 60$. The deconfinement time was estimated in [18] as

$$\tau_{dc} \sim 2R/u_j \sim (R/c_{sc})(\rho_2/\rho)^{1/2}, \tag{2.8}$$

where u_j is the initial plasma jet (liner) velocity, ρ_2 and ρ are density values of the compressed liner and target (at the liner - target interface), correspondingly, and $c_{sc} = (2T_{ign}/m)^{1/2} = 8.78 \times 10^7\, cm/s$ is the thermonuclear sound speed. Replacing this value with the actual sound speed in the target $c = \sqrt{(\gamma P/\rho)}$, we obtain the deconfinement time as

$$\tau_{dc} \sim R(\rho_2/\gamma P)^{1/2}. \tag{2.9}$$

This formula predictions will be compared in the next section with computed values of the deconfinement time.

2.2.3 Comparison of Simulations with Theoretical Predictions

In this section, we study the liner - target setup suggested in [18]. A 15 cm thick deuterium liner implodes and compresses the plasma target. The initial inner radius of the liner is 60 cm, which corresponds to the merging radius of plasma jets forming the liner. The initial state of the liner is as follows: the density $\rho = 3.8 \times 10^{-5}\,\mathrm{g/cm^3} = 9.2 \times 10^{18}\,1/\mathrm{cm}^3$, temperature $T = 0.0358\,\mathrm{eV} = 415.4\,\mathrm{K}$, pressure $P = 0.65\,\mathrm{bar}$, velocity $v = 100\,\mathrm{km/s}$, and the Mach number $M = 60$. The total energy stored in the liner is 164 MJ. The plasma target is initially 5 cm in radius, and its initial density, pressure, and temperature are $\rho = 8.3 \times 10^{-6}\,\mathrm{g/cm^3} = 2 \times 10^{18}\,1/\mathrm{cm}^3$, $T = 100\,\mathrm{eV}$ and $P = 640.3\,\mathrm{bar}$, correspondingly. The ideal gas equation of state with $\gamma = 5/3$ was used for the target, and the pressure - temperature relation in the form $P = 2nkT$ accounted the ion and electron pressure of the fully ionized target material.

Simulation verified that the liner density increases proportionally to r^{-2} during the implosion, as predicted in [18] (see Figure 2.2). The liner density profile before the interaction with the target is shown in Figure 2.3. After the contact with the liner, the target was almost adiabatically compressed until it reached the stagnation point at time 6 μs. The fully compressed target radius was 0.73 cm, and the corresponding compression ratio was 6.8. By "almost adiabatic compression" we mean that a small component of the stagnation pressure can be attributed to the shock wave sent by the liner: while the adiabatic compression would result in the stagnation pressure of 9.3 Mbar, the maximum pressure observed in the target was 11 Mbar. In simulations, the liner failed to compress the target to $R = 0.5$ cm, the expected compressed radius of the theoretical model. As the pressure during the adiabatic compression increases proportionally to the fifth power of the compression ratio, smaller target compression led to a much smaller stagnation pressure compared to theoretical model: [18] predicted 64 Mbar for to the compression ratio of ten. The resulting decrease of the fusion energy gain in simulations is analyzed below. The evolution of the liner - target interface near the stagnation point is shown in Figure 2.4. The velocity of the initial target expansion is approximately 0.58 $cm/\mu s$. Below we compare main quantities used in theoretical estimates such as the deconfinement time, the hydrodynamic efficiency, and the fuel burn-up fraction predicted by theory and simulations. Although these quantities are not explicitly used in simulations for obtaining the energy gain, their calculation from simulation data and comparison with theoretical predictions is useful for a better understanding of the theoretical model.

Deconfinement time. Figure 2.5 depicts the evolution of the normalized pressure in the target and the normalized fusion energy in the vicinity of the stagnation point.

It shows that the fusion gain is more than 90% complete after the pressure in the target is reduced by the factor of two. This justifies the definition of the deconfinement time given above. The deconfinement time calculated from this pressure plot is equal to 220 ns, which is 2.2 times bigger than the estimate of [18]. Formula (2.9), applied to computed target - liner properties at stagnation, gives the deconfinement time of 114 ns while the left hand side of formula (2.8) ($2R/u_j$) gives the value of 146 ns. Both theory and simulations results are significantly different from estimates obtained with a converging shock model [2] which are of the order of 1 μs.

Hydrodynamic efficiency. The hydrodynamic efficiency calculated using the simulation data and formula (2.6) gives the value of 0.016. The corresponding theoretical value reported in [18], obtained using (2.7), is 2.5 times larger: $\eta = 0.04$

Fuel burn-up fraction. The total number of fusion neutrons, obtained in simulations during the entire target evolution, divided by the total initial number of atoms in the target gives the value of the burn-up fraction as 6.67×10^{-4}. The corresponding theoretical prediction is 16.5 times bigger: [18] reports 0.011. The reason for such a big discrepancy is that, despite the longer deconfinement time, the temperature in the target remains well below 10 keV. Even at the maximum compression, only small central spot in the target reached the temperature higher than 10 keV while the volume averaged temperature $\overline{T} = \int_0^R T(r)r^2dr / \int_0^R r^2dr$ was only 5.2 keV.

Distributions of density, pressure, and temperature at the stagnation point are shown in Figures 2.6.

Fusion energy gain. The total fusion energy gain achieved in the simulation was 0.012. This value is 10.8 times smaller than the theoretical prediction. The value reported in [18] is 0.026 using the coefficient 0.2 as the electromagnetic efficiency of the plasma gun. Since we do not consider specific values of the electromagnetic efficiency in this work, the corresponding theoretical value is 0.13. Such a large discrepancy between the theory and simulation is due to the failure of the liner to compress the target to the radius of 0.5 cm and can be easily explained by the theoretical scaling law. Assuming that the fusion reactivity in the vicinity of the ignition temperature scales as T^2, we can derive from (3) and (4) that the fusion gain scales as

$$G \sim P\,\tau_{dc}\,\eta_h. \tag{2.10}$$

Comparing the stagnation pressures, deconfinement times and hydrodynamic efficiencies of the theoretical model and simulation, we conclude that the scaling law predicts 6.5 times smaller fusion gain for the compressed target achieved in the simulation compared to theoretical prediction. Since the actual gain was 10.8 times lower, the discrepancy between the theory and simulation in the sense of the scaling law is approximately 1.7.

To complete the discussion, we also employed the idealized "solid target" model of [18] for the purpose of verification of theoretical predictions. In this model, the plasma target offers no resistance to the liner after the collision of the inner liner surface with the initial target surface. The target freely compresses until it reaches the final compressed state R and then suddenly responds to the liner with infinite resistance. The target pressure sharply increases and reaches the stagnation pressure P_{st}. In the computer code, this process was modeled by inserting a solid ball in the center of the chamber with the radius equal to the compressed target radius of $R = 0.5$ cm. The solid target model was used to compute the dependence of the logarithm of the ram pressure amplification factor A vs. the logarithm of the compressibility factor $C = r_m/R$. Results are summarized in Figure 2.7. We define the ram pressure amplification factor as

$$A = \frac{P_{\text{st}}}{\rho_m * V_m^2},$$

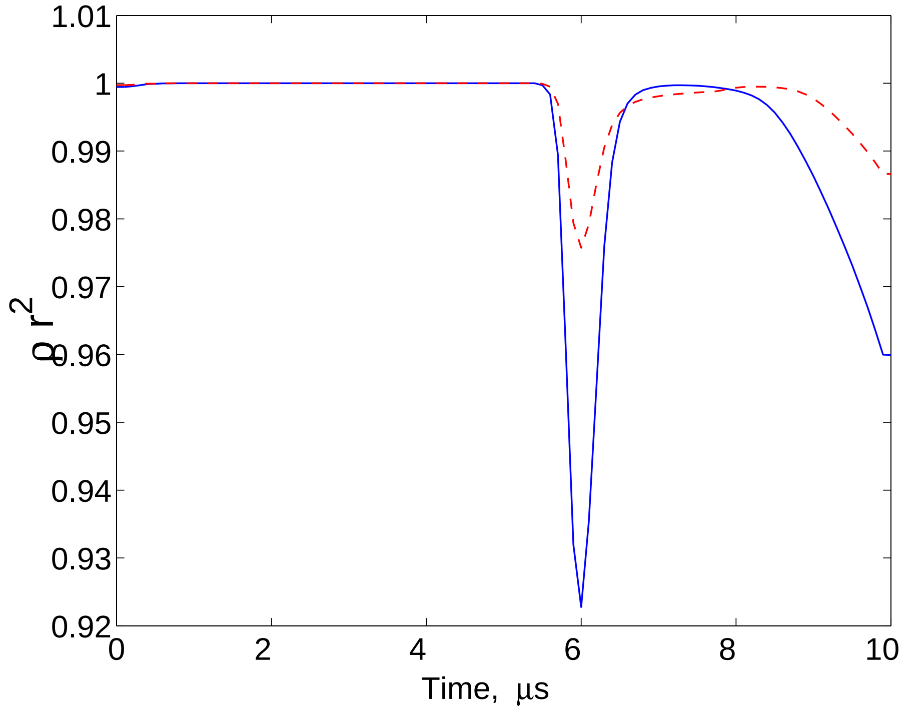

Figure 2.2: Verification of the density scaling $\rho \sim 1/r^2$. Solid line: maximum density in the liner; dashed line: average density across the liner.

where ρ_m and V_m are the initial density and velocity of the liner (or density and velocity of plasma jets at the merging radius). In agreement with theoretical predictions, plots of the simulation data never exceed the ideal line $A = C^2$ (line 1 in Figure 2.7). According to the theory, A initially increases as C increases and then diverges from the ideal line towards saturation (constant A) regime. Such a behavior was obtained for the $M = 60$ liner with adiabatic index $\gamma = 5/3$ (curve 3). Simulations at Mach number 60 and $\gamma = 1.3$ have not reached the saturation at realistic values of the compressibility factor (curve 2). In numerical simulations with low Mach number liners (M = 20), A reached its maximum value at some radial compression value ($\log_{10} C \simeq 2.15$), and then slightly decreased. In agreement with the theory, the point of divergence from the monotonic increase of A can be increased by increasing of the Mach number or reducing of the adiabatic index γ.

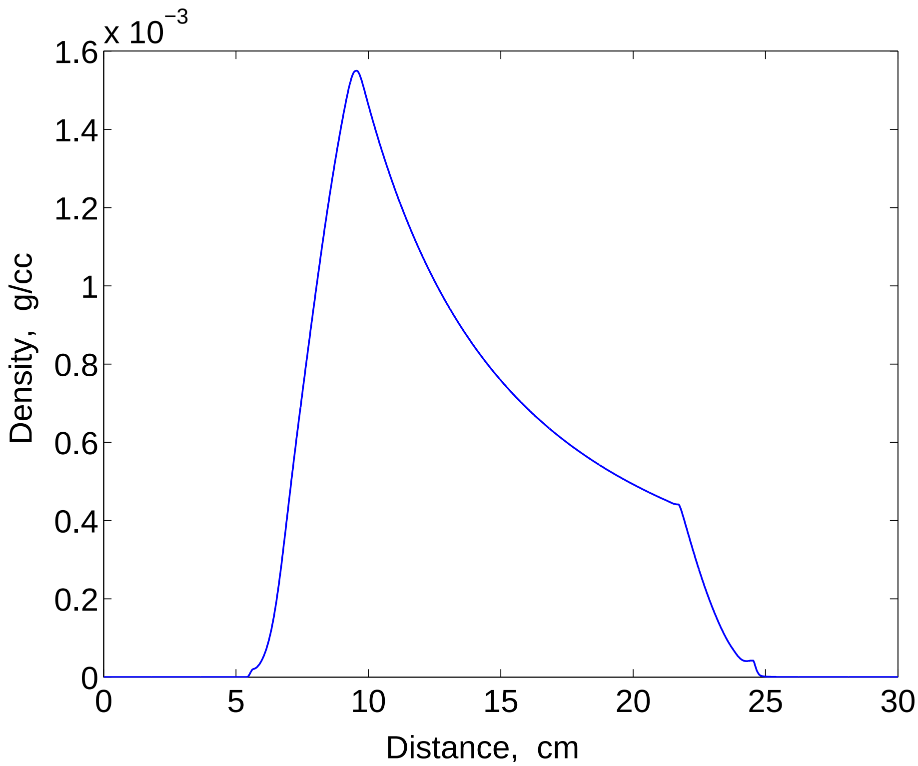

Figure 2.3: Density profile of the DT liner before the interaction with the target.

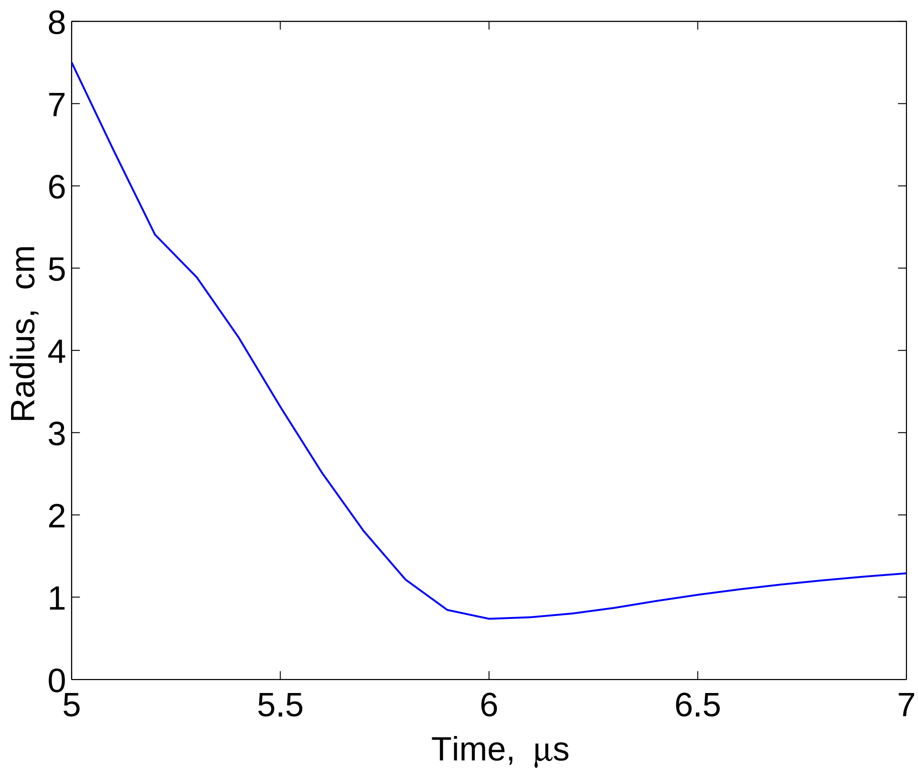

Figure 2.4: Evolution of the liner - target interface near the stagnation point for DT liner with initial thickness of 15 cm.

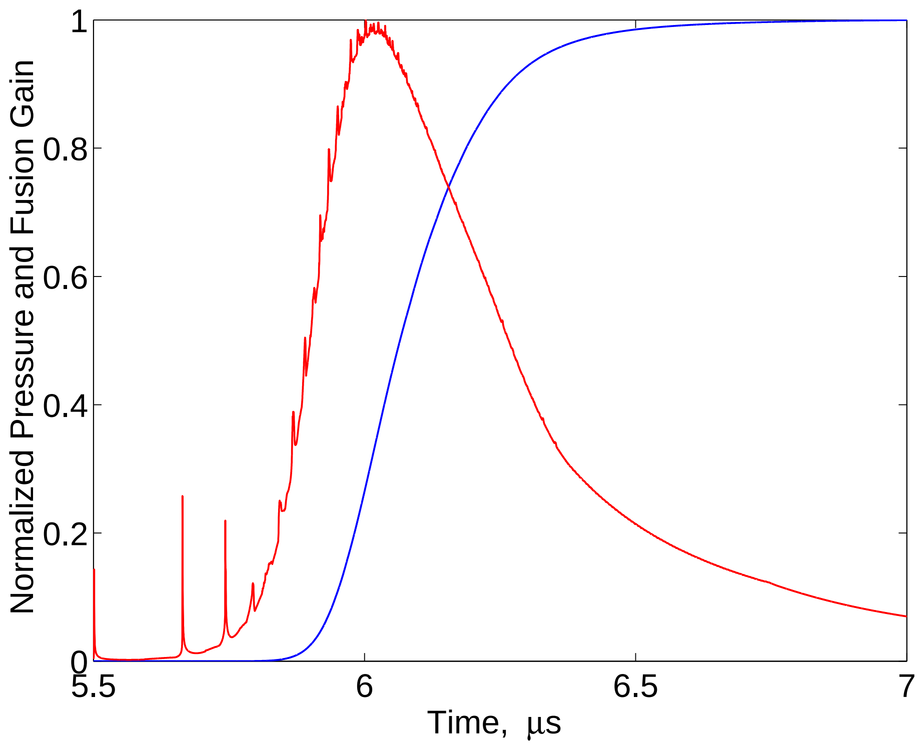

Figure 2.5: Evolution of normalized pressure and normalized fusion energy during target deconfinement for DT liner with initial thickness of 15 cm.

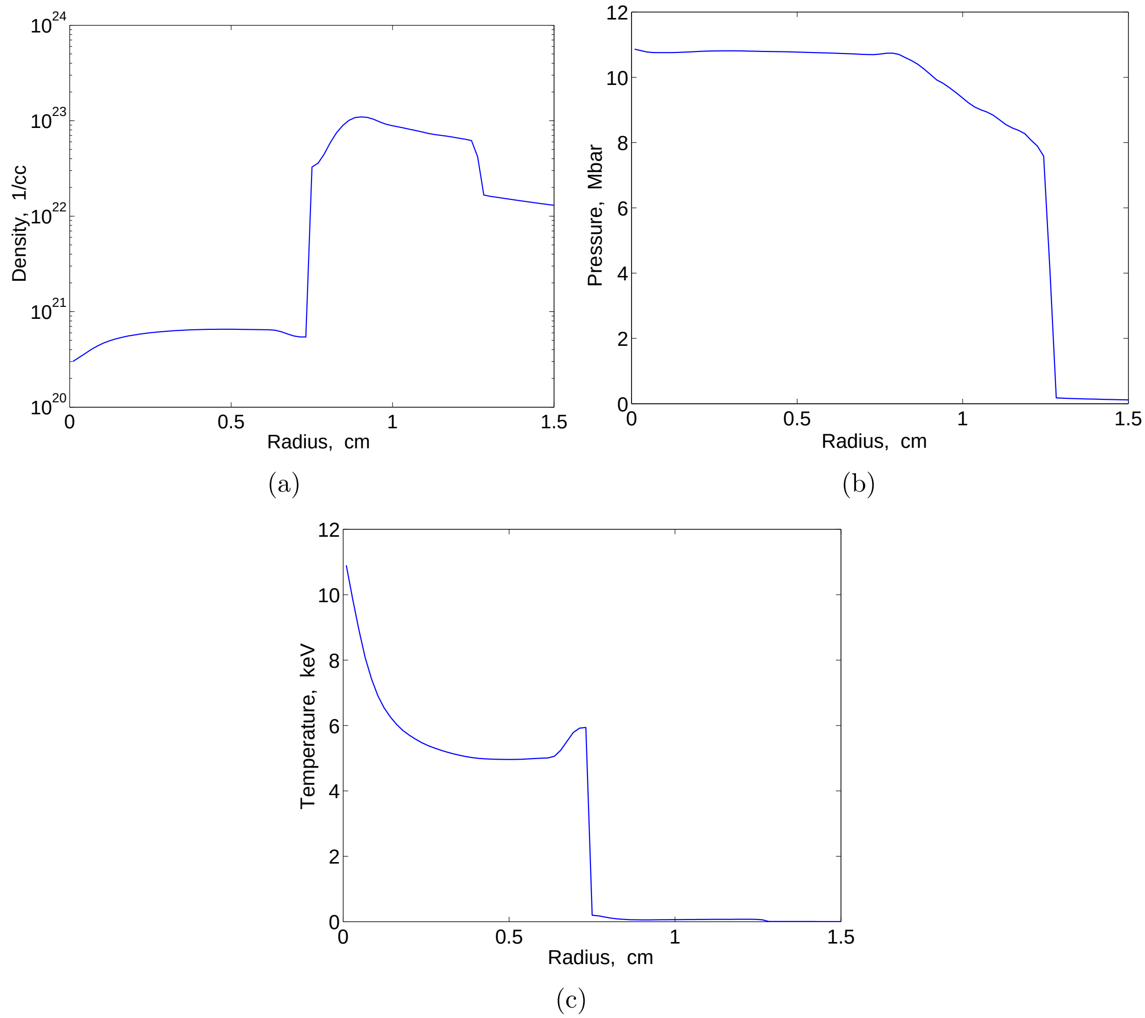

Figure 2.6: Density, pressure and temperature at maximum target compression for DT liner with initial thickness of 15 cm.

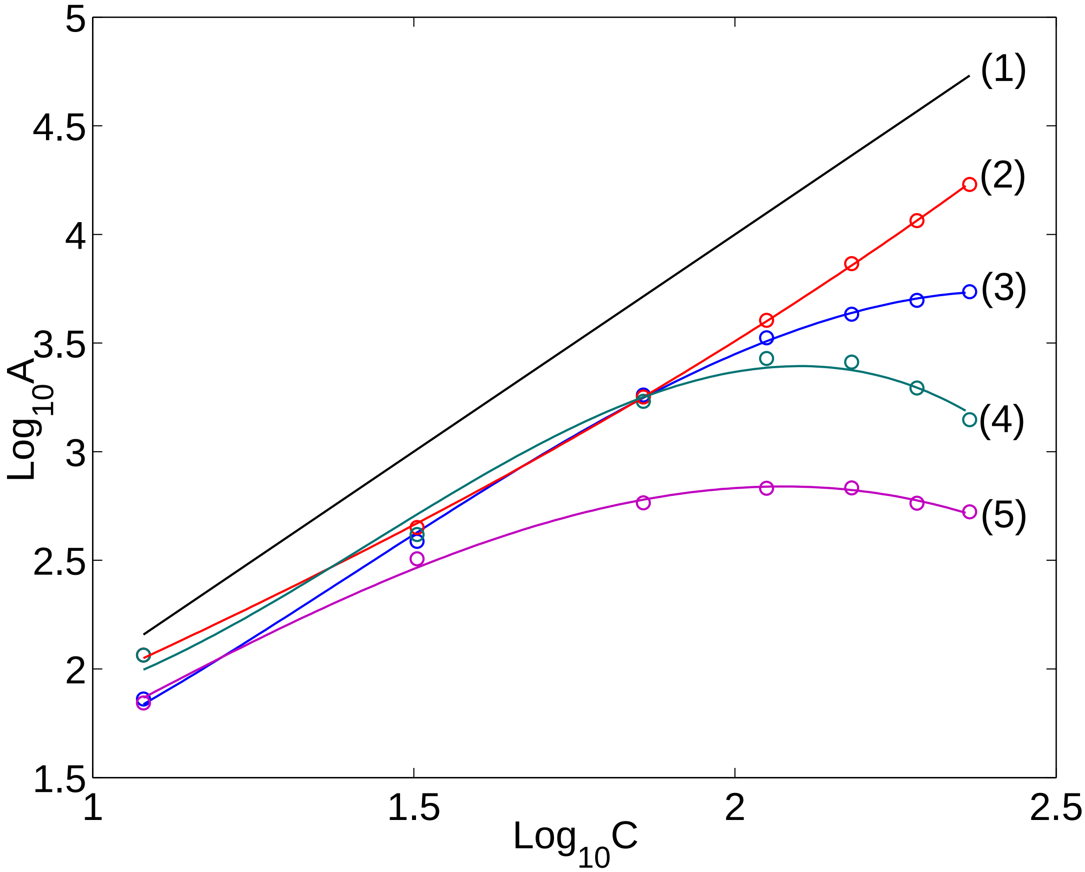

Figure 2.7: Logarithm of the ram pressure amplification factor A vs. logarithm of the radial compression C. Plot (1) corresponds to the ideal model $A = C^2$. Other plots obtained using simulation data. (2): Mach number 60 and adiabatic index $\gamma = 1.3$, (3): Mach number 60 and $\gamma = 5/3$, (4): Mach number 20 and $\gamma = 1.3$, and (5): Mach number 20 and $\gamma = 5/3$. Circles represent numerical simulation data points and solid lines represent the least squares fit of numerical data by cubic polynomials.

2.2.4 Scaling Laws and the Fusion Gain Improvement

In this section, we investigate a possibility of improving the fusion energy gain by varying target and liner parameters within reasonable limits. Theoretical predictions of the impact of parameters on the fusion gain is summarized in the scaling law derived from Parks formulas [18]:

$$G = 10^{-4}\frac{<\sigma v>_{DT}}{T^{3/2}}\frac{R^2}{L_{\text{jet}}}(n_0 n_L)^{1/2}\left(\frac{m_{\text{jet}}}{2.5}\right)^{1/2} C_L C_T^{3/2}\frac{\eta_E}{0.25} \tag{2.11}$$

$$= 10^{-4}\frac{<\sigma v>_{DT}}{T^{3/2}}\frac{r_m\, R_0}{\sqrt{R}L_{\text{jet}}}(n_0 n_L)^{1/2}\left(\frac{m_{\text{jet}}}{2.5}\right)^{1/2}\frac{\eta_E}{0.25}$$

where T and R are the target temperature and radius at stagnation (cm), n_0 is the initial target density (cm^{-3}), L_{jet} is the length of jets forming the liner (cm), n_L is the initial liner density (cm^{-3}), m_{jet} is the jet ion mass (amu), $C_L = R_m/R$ is the radial convergence of the liner, $C_T = R_0/R$ is the radial convergence of the target, and η_E is the electric gun efficiency which is equal to one throughout this paper.

As (2.11) suggests, the fusion energy gain increases with the reduction of the liner thickness provided that such a liner is still capable of compressing the target. A thin liner carries less initial kinetic energy and increases the fusion energy gain by higher values of the hydrodynamic efficiency. We performed simulation reducing the liner thickness to 5 cm and leaving other parameters of the previous setup unchanged. Numerical results showed that the 5 cm deuterium liner has the same ability to compress the target to the fusion condition: the compressed target radius as well as profiles of the temperature, density and pressure at stagnation, and the evolution of pressure (deconfinement time) are practically identical to those for the 15 cm liner. A small difference in details of the thermodynamic profiles at stagnation contributes to 1.9% decrease of the total fusion energy of the target compressed by the 5 cm liner.

In agreement with the scaling law, the fusion gain increases by 3.4 times compared to the 15 cm liner. Notice that the increase of the length of plasma jets forming the liner is not identical to the increase of the liner thickness in a 1D model and the 15 cm thick liner carries 3.5 times larger kinetic energy compared to 5 cm thick liner. Further reduction of the liner thickness for the purpose of the fusion gain increase is not practical as the propagation of very short plasma jets prior to their merger will result in the spreading of their density.

In the previous section, we assumed that alpha particles produced in the nuclear fusion process escape the target without interaction with the target material. Here we employ a very simplified model for the absorption of alpha particles in order to evaluate its effect on the target temperature, pressure, and the fusion energy gain. We assume that some fraction of alpha particles are absorbed locally and deposit their energy of 3.5 MeV per alpha particle. Numerically, we added the energy of the alpha particles to the same computational cells where particles were created. We used 0.35 as the alpha particle absorption coefficient in most of simulations. Anticipating larger burn-up fractions of targets, we also reduced the density of the target at each time step proportionally to the reaction products that left the target.

The inclusion of alpha particle heating had very small effect on the stagnation state and fusion gain of the target compressed by the 15 cm thick deuterium-tritium liner. While the stagnation state was practically identical in both cases, the alpha heating resulted in slightly higher values of the pressure and temperature during the deconfinement process and contributed to the fusion gain increase of 4.3%. As we will see later, the alpha particle heating has much bigger effect on large targets compressed by heavy xenon liners.

In the next simulation series, we replaced the deuterium liner with a 5 cm thick xenon liner with density $\rho = 8.5 \times 10^{-4}\,\mathrm{g/cm^3} \simeq 4 \times 10^{18}\,\mathrm{1/cm^3}$, temperature $T =$

2.27 eV, pressure $P = 14.2\,\text{bar}$, velocity $v = 100\,\text{km/s}$, and Mach number $M = 60$. The total kinetic energy of such a liner is 1 GJ. We also increased the initial target radius to 10 cm. The heavy liner compressed the target to R = 0.84, slightly exceeding the compression ratio of 10. The pressure reached 265 Mbar but some transient pressure peaks associated with the focusing of shock waves during the target compression reached 287 Mbar. The volume averaged temperature was 32.6 keV while the temperature in the target center reached 65 keV. The alpha heating caused slight increase of the averaged temperature during early stages of the target expansion. The highest averaged temperature of 36.8 was reached at 6.3 μs or 300 ns after stagnation. Since the deconfinement time was 200 ns, the highest temperature was reached at $1.5\tau_{dc}$. The computed value of the deconfinement time agrees reasonably well with the theory: $2R/u_j = 168$ ns while formula (2.9) gives 141 ns. The inclusion of alpha heating and the resulting increase of temperature after stagnation does not require modifications of the definition of deconfinement time: the nuclear fusion process was completed by 84% when the pressure dropped by half. The fusion gain obtained in simulations was 2.6 or 217 times bigger compared to the 15 cm deuterium liner setup. The scaling law (2.11) predicts the fusion gain of 12.8.

Keeping the liner unchanged, we performed a series of simulations by increasing the target radius to 30 cm with 5 cm increments. The dynamics of the corresponding fusion gains is plotted in Figure 2.8. We observed that the 20 cm target was the most optimal for the given liner: it achieved the compression ratio of 10, the stagnation pressure of 130 Mbar (the pressure increase is higher than predicted by the adiabatic compression law because of the alpha heating), the average temperature of 16 keV, and produced the fusion gain of 10. Alpha heating caused further increase of the target temperature during deconfinement and the average temperature reached the maximum value of 23.3 keV at 200 ns after the stagnation. The computed value of the deconfinement time was 150 ns and theoretical predictions are as follows: $2R/u_j = 400$ ns while formula (2.9) gives 360 ns. The profiles of density, pressure, and temperature at stagnation and 200 ns after stagnation are shown in Figure 2.9. The value of the fusion gain calculated from the scaling law (2.11) is 30. The interplay between the target size, compression ratio, and the stagnation temperature led to smaller values of the fusion gain for smaller and bigger targets: $G = 6.7$ for 15 cm radius target, $G = 7.0$ for 25 cm target, and $G = 2.5$ for 30 cm radius target in the presence of alpha heating. While the small target size was the critical factor for 10 and 15 cm targets, smaller stagnation temperatures for 25 and 30 cm targets contributed to reduced fusion gains. In order to evaluate the effect of alpha heating for targets producing significant energy gains, we performed the same series of simulations with the alpha heating turned off. Results are illustrated in Figure 2.10. The absence of alpha heating reduced the fusion gain of 15 cm target to 5.6 while the fusion gain for 20 cm target was reduced to 6.0. The corresponding theoretical value for the 20 cm target obtained from (2.11) is 27.6. Therefore the scaling law predicts approximately 4 times higher fusion gain compared to simulations because higher target compression rates are assumed in theoretical estimates.

It was suggested in the original paper on the plasma jet MIF [25] that the inner layer of a composite liner containing deuterium-tritium inner part and an outer xenon pusher may provide additional fuel for the thermonuclear reaction. For testing of this idea, we included a 5 cm deuterium layer in front of a 5 cm xenon layer. The initial density was $3.8 \times 10^{-5}\,\mathrm{g/cm^3}$ for the deuterium layer, $8.5 \times 10^{-4}\,\mathrm{g/cm^3}$ for the xenon layer, the initial pressure was 14.2 bar in both layers, and the Mach number was 60 in xenon and 12.5 in deuterium, correspondingly. The liner was used to compress the 20 cm radius target that gave the highest fusion gain for the single-layer xenon liner. Because of high pressure and much lower Mach number in the deuterium layer compared to the single deuterium liner simulations, the deuterium layer quickly spread out reaching the thickness of 10 cm before the interaction with the target. Then the process consisted in the compression of both the deuterium layer and the target. At stagnation, the deuterium liner thickness was only 6 mm while the target was compressed to 2.4 cm. Because of the compression of the deuterium liner layer, the pressure in the target reached only 57 Mbar while the average temperature in the target was about 14.5 keV. Without α-heating of the liner layer, the released fusion energy was reduced by 2 times compared to the single xenon liner case. The compression of the deuterium layer of the liner raised the temperature in the liner at the target - liner interface to 4.5 keV at stagnation and the temperature was reduced to 1 keV within 2 mm. Therefore the fusion energy production in the deuterium layer was negligible without the α-heating. The state of the target at stagnation is shown in Figure 2.12. The use of the composite deuterium - xenon liner also reduced the fusion production of the 10 cm target by 2 times and 30 cm target by 1.5 times. In future work, the effect of alpha heating of the inner liner layer will be addressed.

2.2.5 Conclusions

Using the method of front tracking, we have performed spherically symmetric simulations of the implosion of plasma liners and compression of targets related to the plasma jet driven magneto inertial fusion. The study of the ram pressure amplification factor A and its dependence on the radial compressibility $C = r_m/R$ is in good agreement with theoretical predictions. Simulations of a deuterium-tritium target with the initial radius $r = 5$ cm, density $n = 2 \times 10^{18}\,1/\text{cm}^3$, and temperature 100 eV, compressed by a 15 cm thick deuterium liner with the initial radius of 60 cm, density of $9.2 \times 10^{18}\,1/\text{cm}^3$ and Mach number 60, have been compared in details with theoretical predictions of [18]. Simulations showed that such a liner will not be able

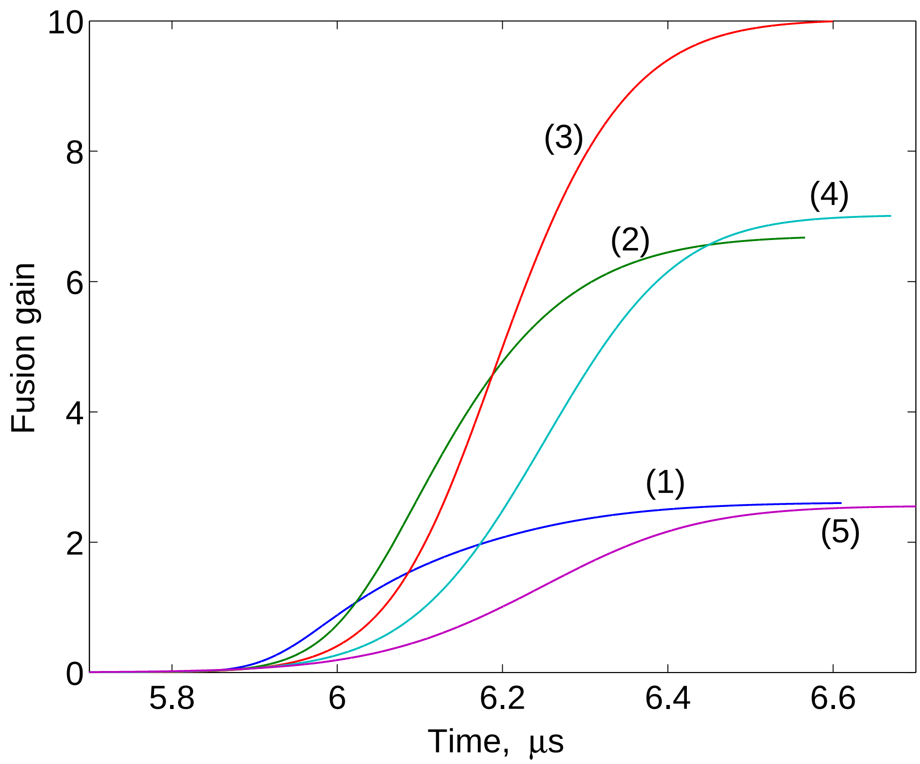

Figure 2.8: Dynamics of the fusion gain of targets compressed by 5 cm thick single layer xenon liner. Initial target radii are: 10 cm (1), 15 cm (2), 20 cm (3), 25 cm (4), and 30 cm (5).

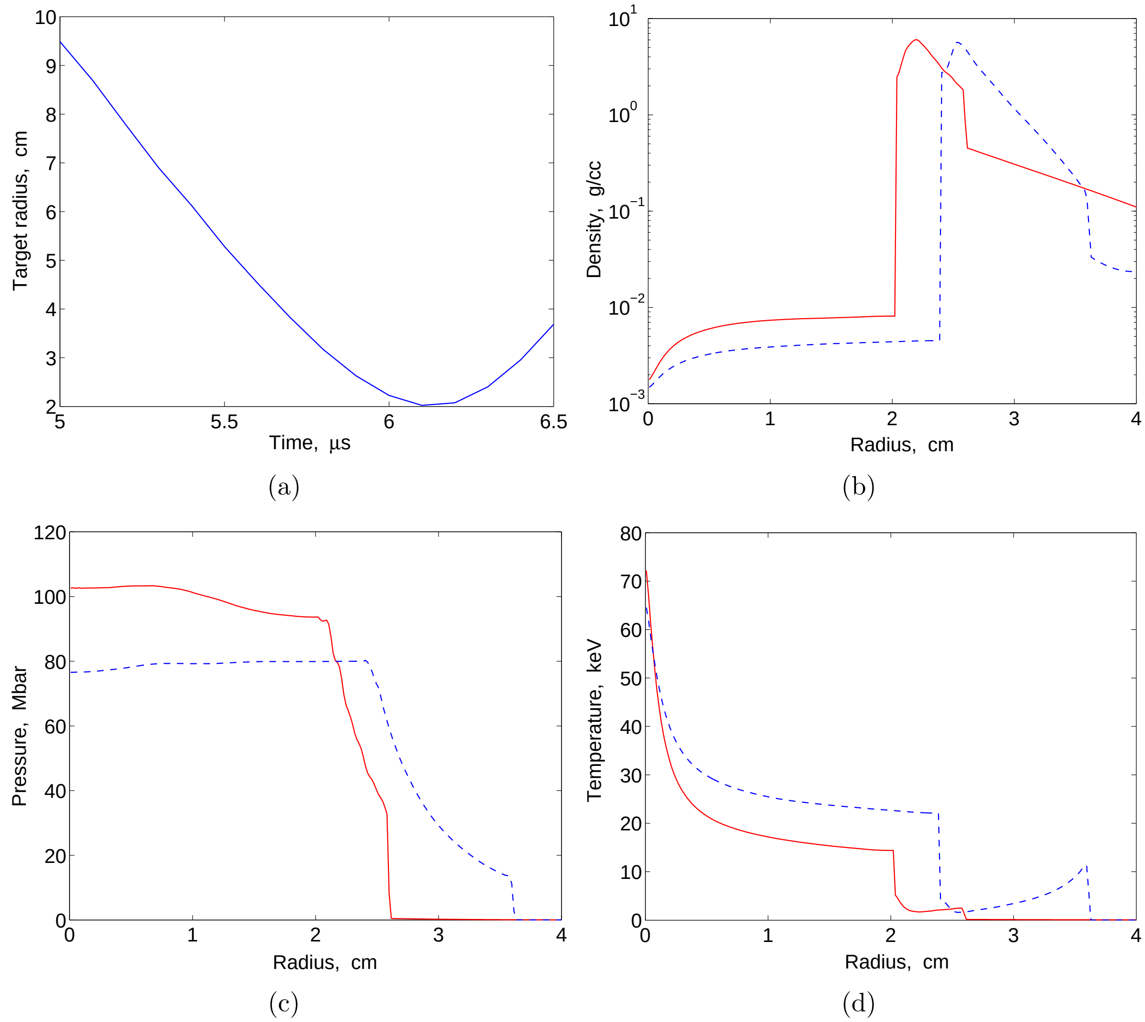

Figure 2.9: Target surface evolution (a) and density (b), pressure (c), and temperature (d) at stagnation (solid line) and 200 ns after stagnation (dashed line) of initially 20 cm target compressed by the 5 cm thick xenon liner.

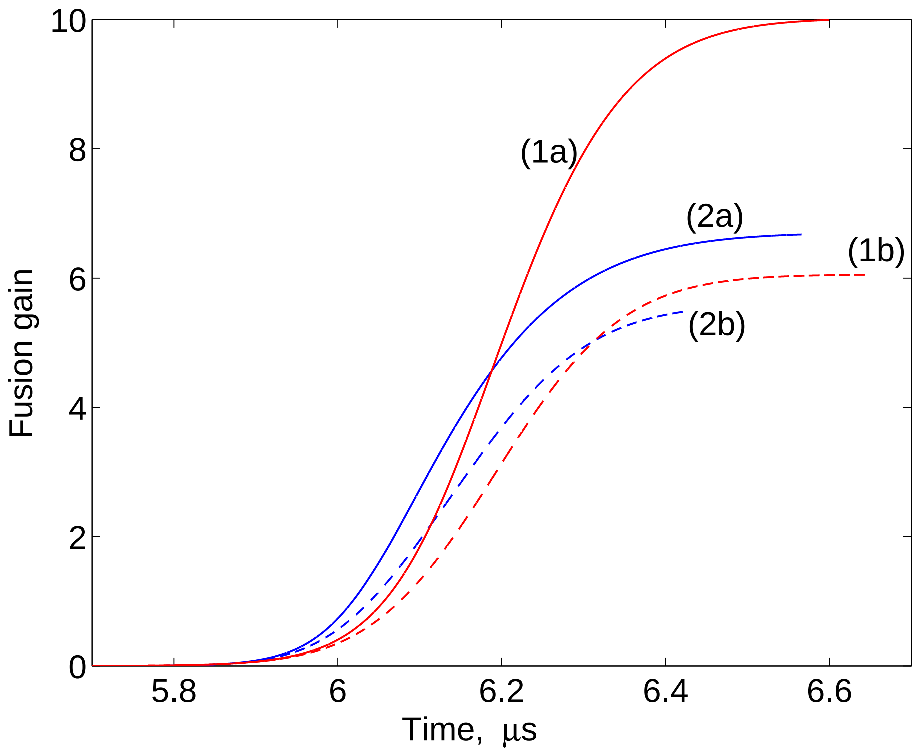

Figure 2.10: Influence of alpha heating on the fusion gain of targets compressed by 5 cm thick single layer xenon liner. Solid lines show the fusion gain in the presence of alpha heating and dashed lines show the fusion gain when alpha heating was turned off. Initial target radii are: 20 cm (1a,b) and 15 cm (2a,b).

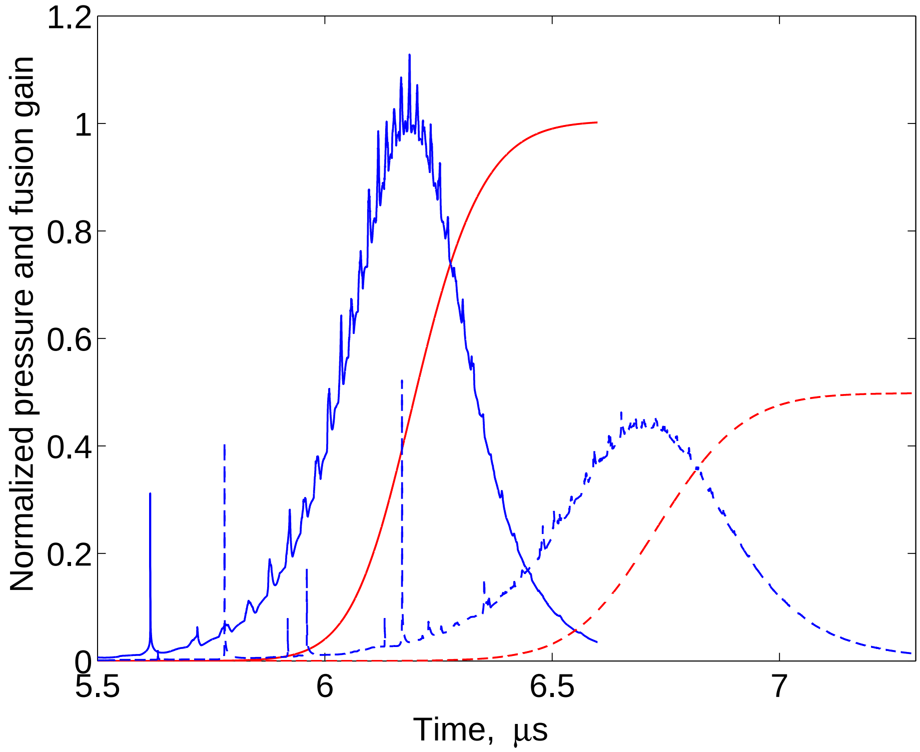

Figure 2.11: Normalized pressure and fusion gain of the 20 cm target compressed by the single 5 cm thick xenon liner (solid line) and the composite liner containing 5 cm thick interior deuterium-tritium layer and 5 cm thick outer xenon layer.

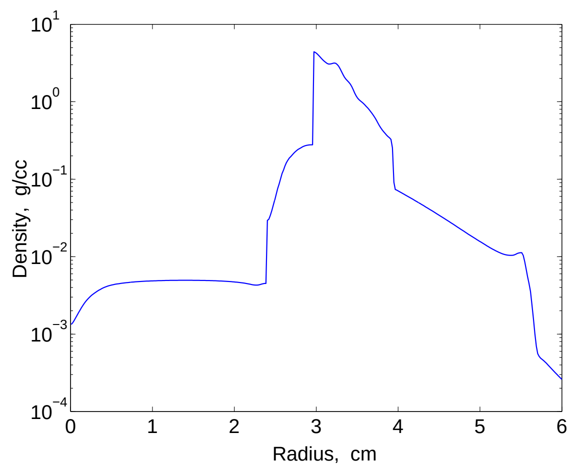

(a)

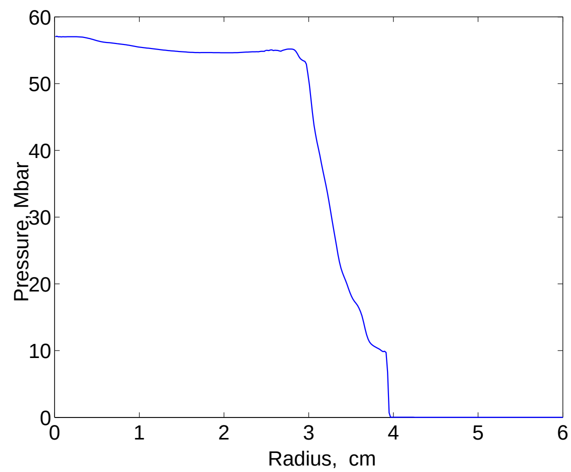

(b)

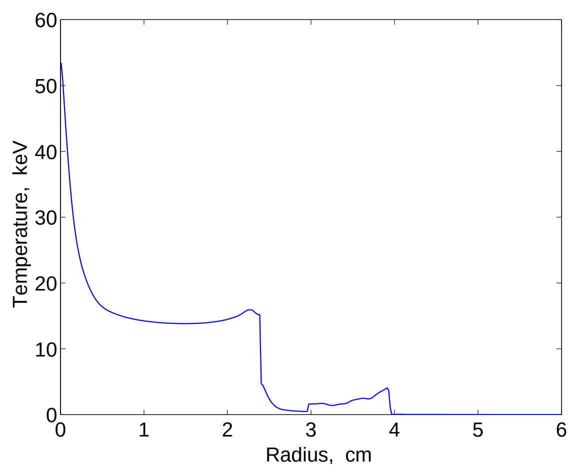

(c)

Figure 2.12: Density (a), pressure (b), and temperature (c) at stagnation (solid line) and 200 ns after stagnation (dashed line) of initially 20 cm target compressed by the composite deuterium - xenon liner.

to achieve the compression rate of 10 obtained in the theoretical work. In simulations, the target was compressed to $R = 0.73$ cm at stagnation. It reached the pressure of 11 Mbar and produced 10.8 smaller amount of the fusion energy compared to the theory. However when the theoretical scaling law was used to estimate the fusion gain of the target compressed by 6.8 times to the stagnation radius of 0.73 cm, the disagreement with the theory was only by the factor of 1.7. Simulations showed that the inclusion of alpha particle heating had very small effect on the fusion gain in this liner - target setup: the local deposition of the energy of alpha particles using the absorption coefficient of 0.35 increased the fusion gain by only 4.3%. In agreement with the scaling law, the fusion energy gain increased with the reduction of the initial liner thickness to 5 cm since such a liner, while carrying 3.5 times smaller kinetic energy, has the same ability to compress the target as a much thicker one: the profiles of pressure, density and temperature at stagnation and the deconfinement time are practically identical to ones obtained with 15 cm thick liner. Further reduction of the liner thickness seems impractical because of the diffusion of short plasma jets during their propagation from the plasma gun to the merging point.

We have also investigated the fusion gain produced by larger targets compressed by heavy xenon liners and double layer deuterium - xenon liners. With the inclusion of alpha heating, the fusion energy gains significantly improved and reached 10 in the most optimal setup for a given chamber size: 20 cm radius target compressed by a single layer xenon liner. The theoretical formula for the fusion gain predicts approximately 4 times higher fusion gain compared to simulations because the theoretical target compression rates are higher. For all simulations, deconfinement times calculated from simulation data agreed within the factor of two with theoretical formulas of [18] and were significantly lower compared to estimates of the order of 1 μs obtained with the converging shock model of [2].

Turning off the alpha particle heating reduced the fusion gain by 1.7 times. The double layer deuterium - xenon liners, expected to provide extra fuel for the thermonuclear reaction, have been simulated as well. Because of the compression of the deuterium liner layer, the compression ratio of the target decreased. Without the α-heating of the inner liner layer, the fusion gain was twice smaller for the 20 cm target. Similar reductions were observed for different target sizes. Simulations showed that the compression of the inner liner layer is not sufficient to achieve the ignition without α-heating. This effect will be investigated in the future work.

Chapter 3

Cylindrically Symmetric Simulation of Detached Jet

In this section, we simulate the propagation of plasma jets from the nozzle of the plasma guns to the merging radius. The purpose of this simulation is to calculate the distribution of density and pressure in plasma jets before their merging. The initial conditions of the jet depends on some complex processes in plasma guns and are not known exactly. As the research on plasma guns continues, these questions will be clarified. For this study, we assume constant states.

The plasma jet runs more than 5 meter with velocity 100 km/s in the chamber. We use the following initial condition: Mach number = 60, $\rho = 3.8\text{e-}5\ g/cm^3$, pressure = 0.6332 bar, R = 41.3. Ambient gas is high vacuum with $\rho \sim 10^{-10}\ g/cm^3$, pressure $\sim 10^{-6}\ bar$. We use 2-dimensional cylindrical coordinate system which represents the 3-dimensional problem.

Boundary condition are as follows: top and bottom are both flow through boundary condition; left is the reflecting boundary condition; right is the flow through boundary condition. We use reflecting boundary condition, so only half domain is calculated.

In [18], Parks estimated the jet expansion during its propagation from the plasma gun to the merging point. Using the following assumptions

(1) the jet keeps uniform density during expansion;

(2) the length of jet is long enough, $L \gg r$;

(3) the jet expansion speed equal to the sound speed at time = 0.

the jet radium at the merging point is: $b(r_m) = b_0 + c_{s0}(r_c - r_m)/u_j$. Here b_0 is the jet radius when jet leaves the plasma gun; c_{s0} is the initial sound speed; r_c is the chamber radius; r_m is the merging radius. This is a linear expansion model.

We will still keep the assumption 1 and 2. However, expanding velocity is a function of time. Assuming the adiabatic jet expansion,

$$\frac{ds}{dt} = \sqrt{\gamma\frac{P}{\rho}} = \sqrt{\gamma * const * \rho^{\gamma-1}} \tag{3.1}$$

$$\rho = \frac{mass}{\pi * (r+s)^2 * L} \tag{3.2}$$

$$A = \sqrt{const * \gamma * (\frac{mass}{\pi L})^{\gamma-1}} \tag{3.3}$$

$$ds/dt = A * (r+s)^{-2/3} \tag{3.4}$$

$$s(t) = A * t^{3/5} + C_1, s(0) = 0$$

$$t = (r_c - r_m)/u_j, r_{jet}(t) = s(t) + 5$$

We can also eliminate assumption 2, so the length of jet should be considered during jet expansion. If we neglect the compression wave in the jet head and the rarefaction in the jet tail, the jet has the same expansion speed in the head as in the tail part. Then the relation between volume and density should be written as:

$$\rho = \frac{mass}{\pi * (r+s)^2 * (L+2s)}$$

Then we need to solve a third order polynomial and only the real root is the solution. To contain sufficient mass, the jet length should be at least 2 times of jet radius. In our simulation we choose the jet length about 4 times bigger than the jet radius, so we still use the first prediction to predict the jet radius.

Let us keep the second assumption and consider that the shape of jet is not a cylinder with flat edges but a cylinder with half sphere ends. Then after substituting all parameters we obtain

$$r_{jet} = ((t + 0.03) * 487.291)^{\frac{3}{5}} \tag{3.5}$$

In figure (3.1) the comparison is shown of Parks' linear velocity prediction, our non-linear prediction and the numerical simulation with the density cut at 0.1*original density.

Strong rarefaction wave behind the detached jet affects the Mach number at the tail of the jet. if we include the jet tail data to calculate the average Mach number, the big Mach number in vacuum behind the jet tail will significantly raise the average Mach number. We only consider the top half of the jet body when we calculate the average Mach number from the numerical data. We also use a weighted method to calculate the average Mach number and average temperature. The weight factor is the density, therefore the center of jet which has a small volume and a big density will play an important role in the average value. We define:

$$\hat{M} = \frac{\int M * \rho}{\int \rho}$$

$$\hat{T} = \frac{\int T * \rho}{\int \rho}$$

The figure (3.2) shows the adiabatic cooling process. The average Mach number

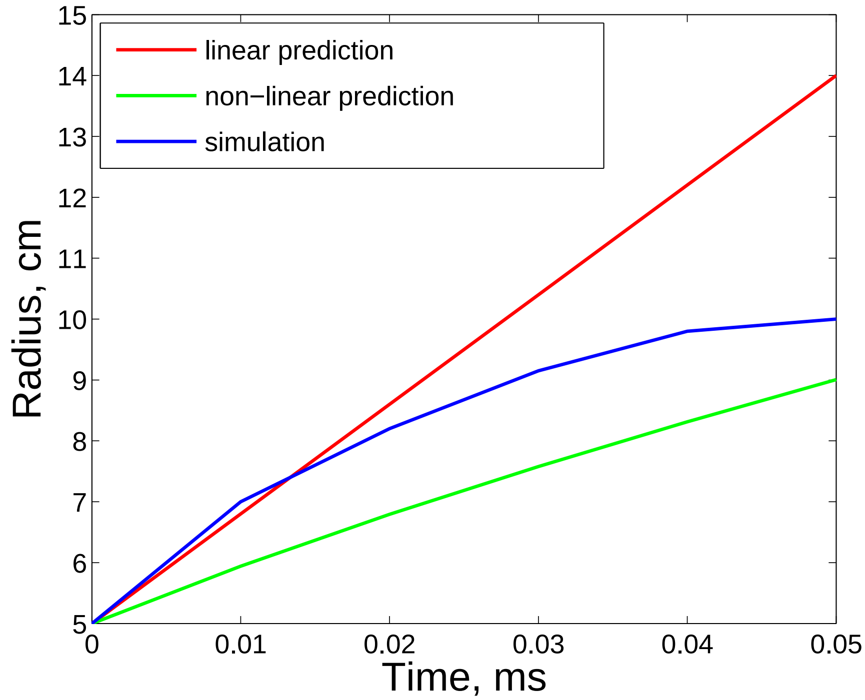

Figure 3.1: Jet expansion.

increases with time and the average temperature decreases with time.

In the remaining part of thesis, we will use weighted average if there is no special note.

The density, pressure and temperature profiles change along the transverse direction in the process are shown in figure 3.4.

The length of jet affects the Mach number in inverse ratio. We compare 2 rectangular jets. One is 10 cm long, another is 20 cm long. The average Mach number of 20 cm jet is smaller than 10 cm jet. When the jet length is increasing, the Mach number will decrease, but the difference is negligible.

In the cylindrically symmetric simulations, we also examined the effect of the boundary condition at the domain edge opposite to the jet axis. In addition to the flow-through boundary condition, we also used other boundary conditions that

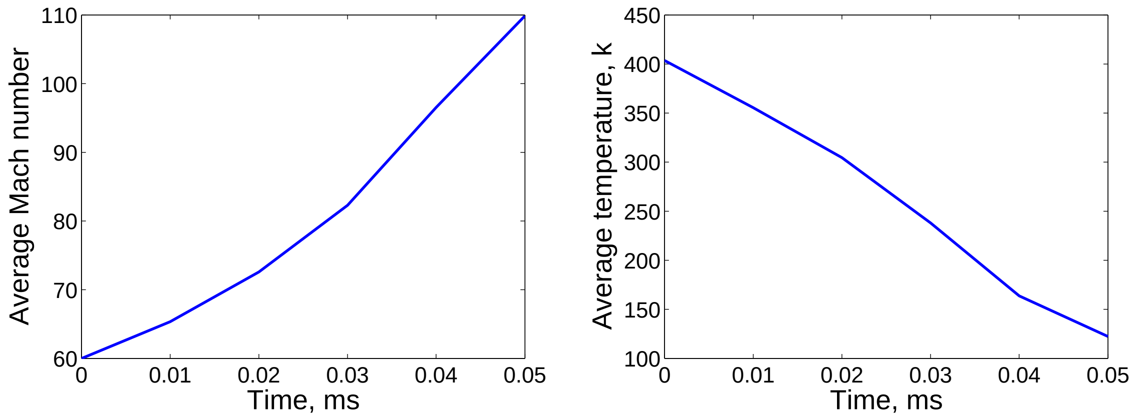

Figure 3.2: Weighted Average Mach number and temperature of detached jet

modeled the presence of another jet at some distance. Simulations showed that the flow-through boundary condition is sufficient for practical purpose.

The jet expansion during the propagation determines the number of jets N that is needed for a given chamber size and the chosen merging radius. Let us assume that at the merging time, the jets will form a liner without holes,

$$\frac{4}{3}\pi r_m^2 = N\pi r_{jet}^2.$$

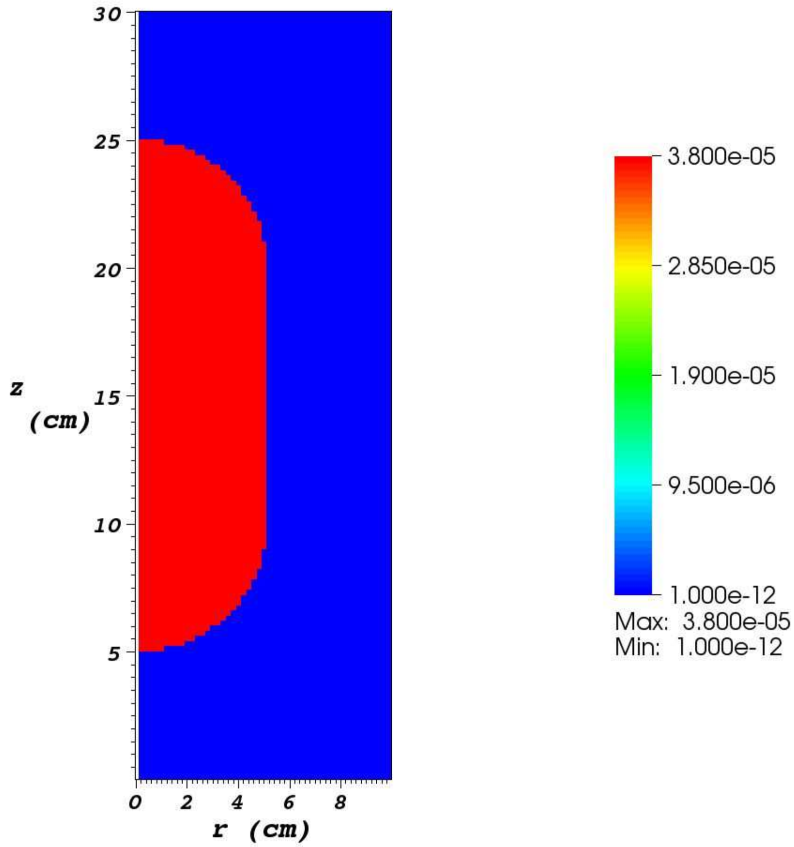
30
25
20
15
10
5
z
(cm)
0
2
4
6
8
r (cm)
3.800e-05
2.850e-05
1.900e-05
9.500e-06
1.000e-12
Max: 3.800e-05
Min: 1.000e-12

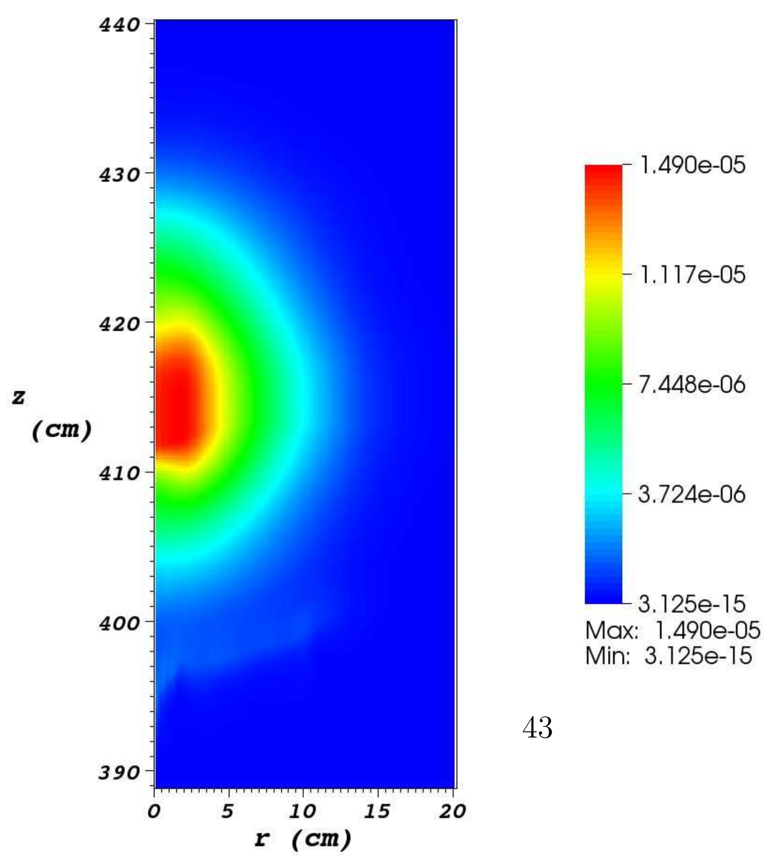
440
430
420
410
400
390
z
(cm)
0
5
10
15
20
r (cm)
1.490e-05
1.117e-05
7.448e-06
3.724e-06
3.125e-15
Max: 1.490e-05
Min: 3.125e-15

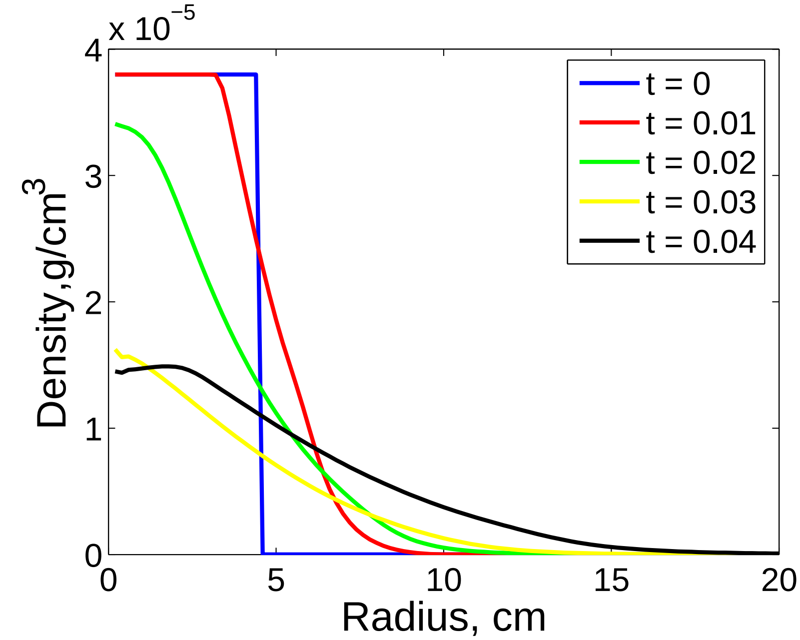
x 10^−5
Density,g/cm^3
Radius, cm
t = 0
t = 0.01
t = 0.02
t = 0.03
t = 0.04

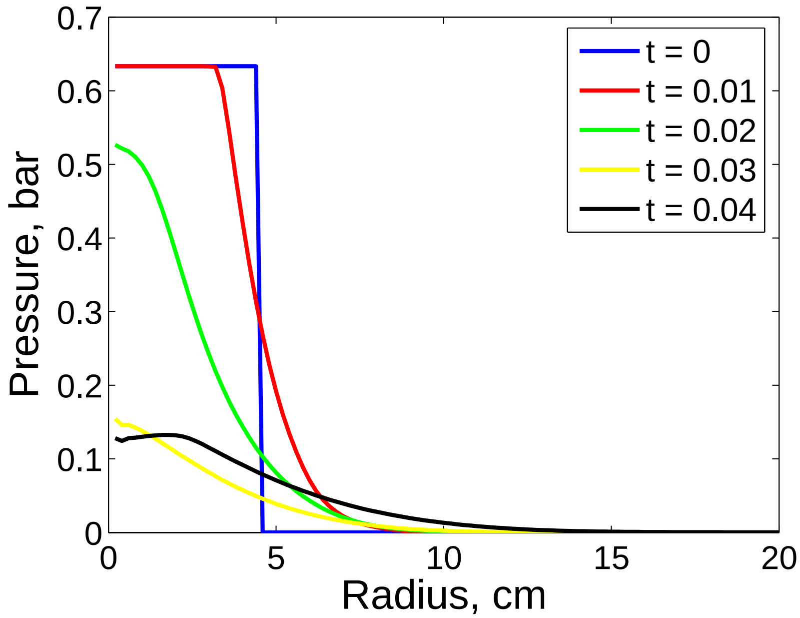
Pressure, bar
Radius, cm
t = 0
t = 0.01
t = 0.02
t = 0.03
t = 0.04

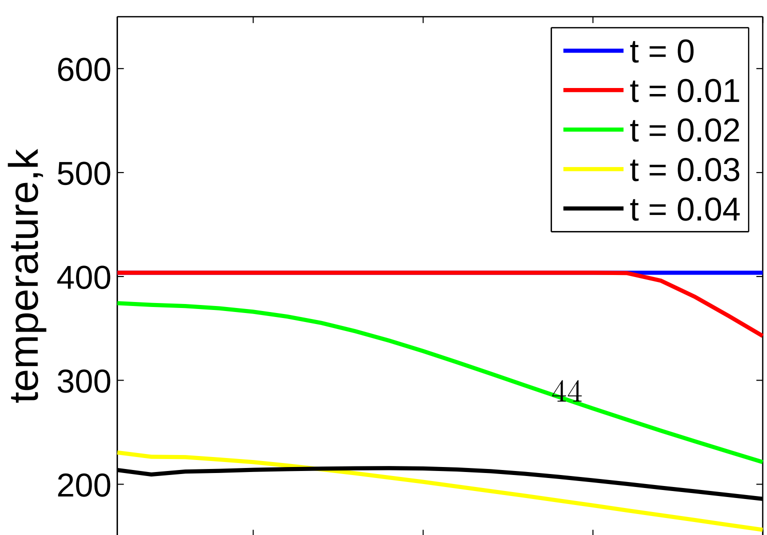
temperature,k
t = 0
t = 0.01
t = 0.02
t = 0.03
t = 0.04

Chapter 4

3D Liner Implosion

4.1 Introduction

In this chapter, we use the results of previous chapter to initialize 3D simulations of the jets merging and liner formation. Simulations were performed on New York Blue using 4096 processors. The purpose of these simulations is to examine the structure of the liner, the uniformity and the reduction of the Mach number during the liner implosion. We also examine the dependence of the liner properties on the number of jets, the merging radius and the chamber size.

We need to initialize the 3D problem with the 2D results from the last chapter, so we need to do a transform from 3D Cartesian coordinates (x, y, z) to 2D cylindrical coordinates (R, Z). We use the following algorithm

Step 1: Find the nearest jet center point (x_0, y_0, z_0), then construct the line from the original point $(0, 0, 0)$ to the nearest jet center point;

Step 2: Find the shortest distance R from (x, y, z) to the line;

Step 3: Find the distance L from (x, y, z) to the original point $(0, 0, 0)$, $Z = \sqrt{L^2 - R^2}$.

Parks [18] studies theoretically th collision of jets with each other at a very small angle and the formation of oblique shocks the flow field. He describes this process

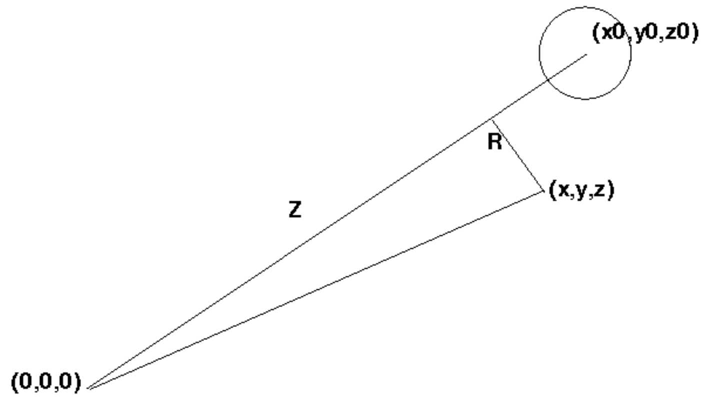

Figure 4.1: Coordinate transform.

as analogous to the supersonic flow past a wedge with a small turning angle. The main oblique shock is on the edges of the jets, so pressure at this shocked region is much larger than in the interior region. Given this fact, he concludes that there will be a sideways rarefaction fan and a series of internal shocks. As a result, Mach number will be reduced as $M = 12.7(\gamma - 0.3)^{4.86}$ because of the oblique shock. This is partially responsible for the hydrodynamic efficiency less than 0.04 in his study because the energy supplied to the system goes mostly into the plasma liner rather than the target plasma.

As we have seen from last chapter, the Mach number increases during the jets propagation step. Our simulations of the detached jets described the profile of jets before the merger. The spreading of jets may significantly decrease the strength of oblique-shock-like compression wave. In this chapter will use three dimensional numerical simulation to answer the question about the Mach number reduction.

4.2 Spherical Centroidal Voronoi Tesselation

In the jet merger 3D simulations, the initial array of N jets must be initialized behind the merging radius with jets distributed uniformly. The problem of the jet placement can be solved using the spherical centroidal Voronoi tesselation.

The SCVT problem (Spherical Centroidal Voronoi Tesselation) distributes N points in the unit sphere surface as uniformly as possible. In general two dimensional centroidal Voronoi tesselation, the purpose is to get the minimum value of the integral of the whole domain point density function using the iteration method. Since SCVT problem should be implemented in a sphere, the problem is solved as a constrained optimization problem. We use the software by John Burkardt that implements Qiang Du's algorithm [6] (old.math.iastate.eduburkardt/f_srcscvtscvt.html).

The result of one simulation that places 70 points on a unit sphere using 200 iterations is shown in Figure (4.2). We checked the error after 200 iterations and obtained a satisfactory result. The distance between any point and its nearest neighbor is almost the same up to 4 significant digits for every other points in the sphere. The increase of the iteration number does not increase the accuracy of the point placement. Firther increase could be obtained by randomly changing the initial point placement and repeating the optimization procedure. It is known that such a problem can not be solved with arbitrary accuracy.

4.3 Merging of jets in the 6-meter radius chamber

In Park's paper, 70 jets were used to obtain $r_m = 60cm$, because the final jet radius before the merger was takes as $r_{jet} = 15cm$. Out simulation of the jet spreading suggests that we need 144 jets.

Figure (4.4) shows the Mach number reduction during merging process. The

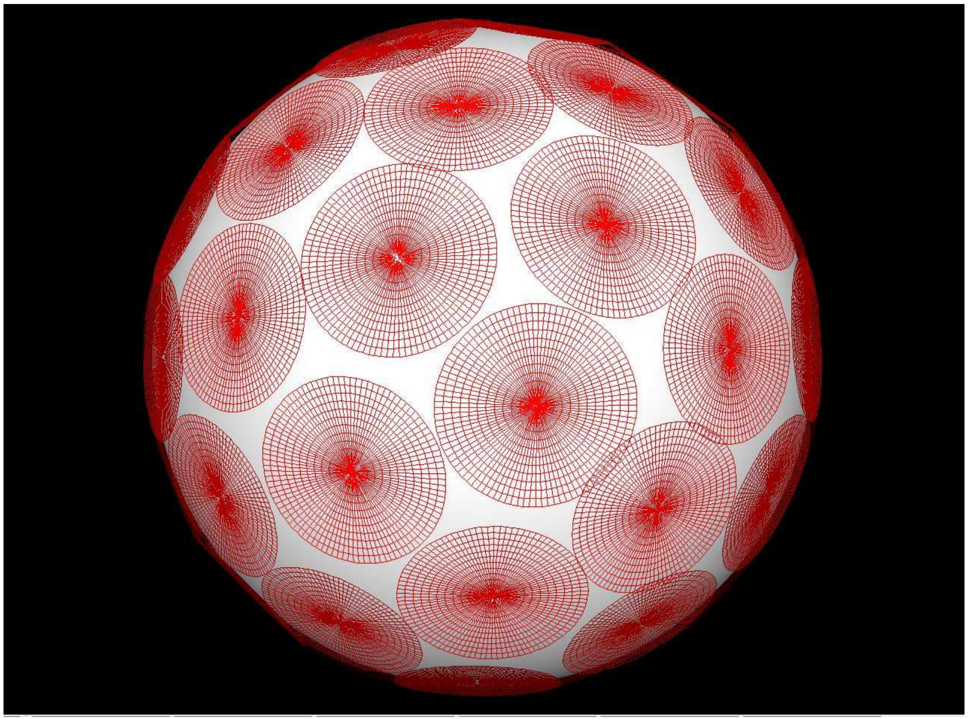

Figure 4.2: SCVT result for 70 points with 200 iterations

Mach number reduces from 100 to 30 during merging. A 800^3 grid is compared with 512^3 grid and comparison shows good convergence on the Mach number reduction.

Before jets are fully merged, the biggest density appears in the center of each jet. However the highest pressure appears at the edge of each jet because of the compression wave. We observe the formation of high pressure contours having shapes of the pentagon, hexagon, etc. This phenomenon is also observed in Charles Knapp's thesis. The density contour figures before and after merging process are shown in Figure 4.6.

4.4 Merging of jets in the 3-meter radius chamber

We will keep the same 2-dimensional input data as in section 2, all the geometry parameters, such as length and radius, and physical parameters,density, pressure, and

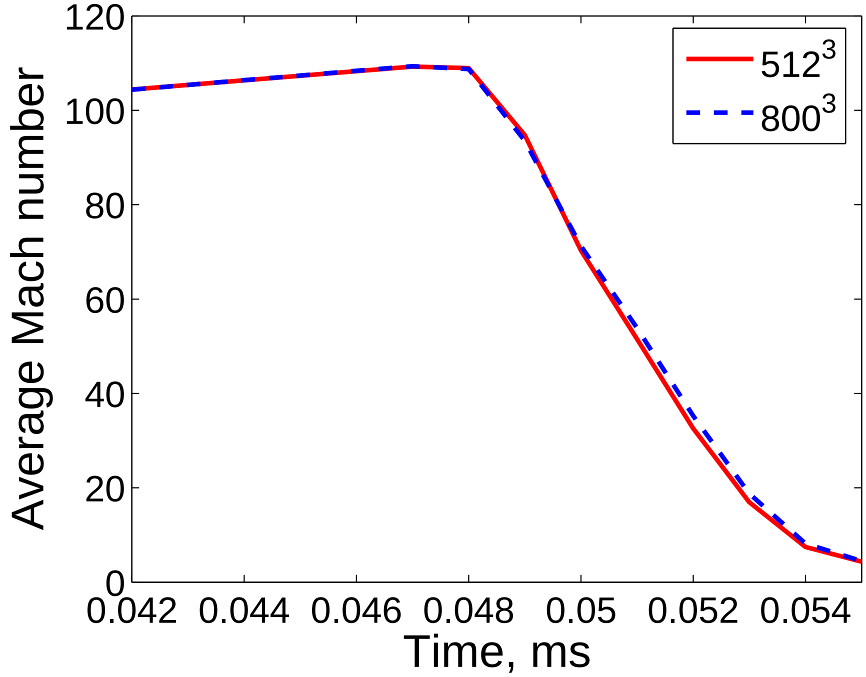

Figure 4.3: Mesh convergence.

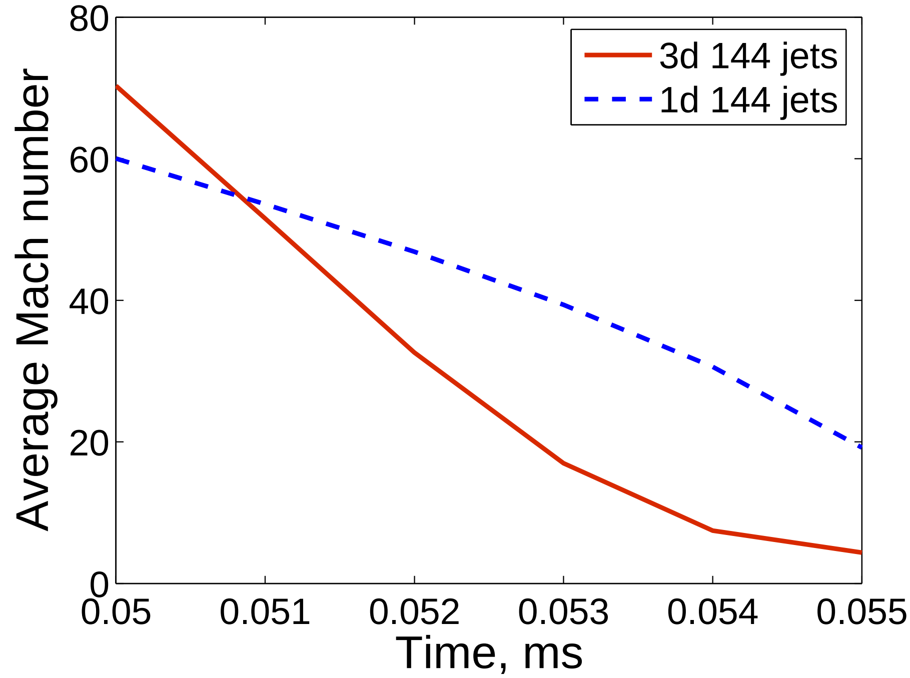

Figure 4.4: Comparison between 1D and 3D average Mach number.

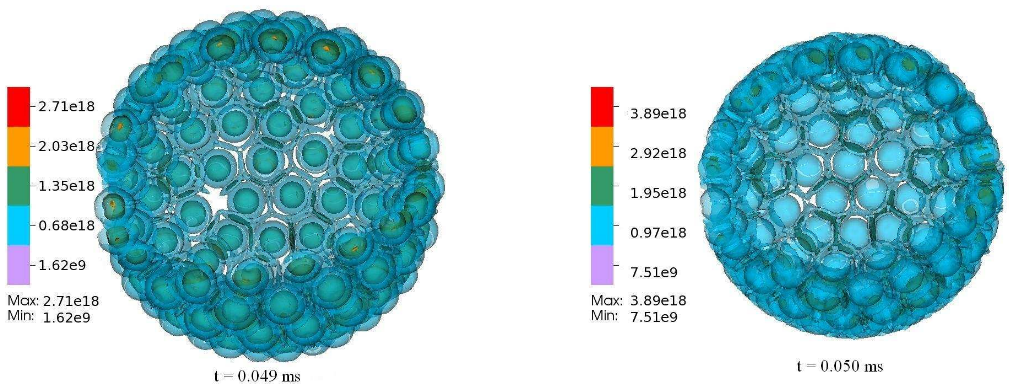

Figure 4.5: Density contour before merging: t= 0.49ms and t=0.50ms

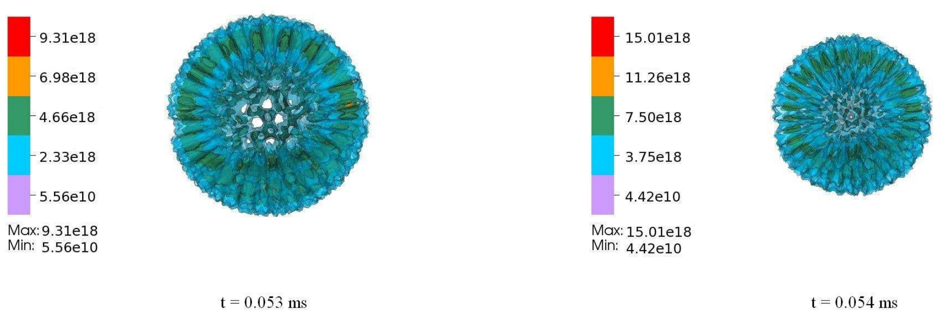

Figure 4.6: Density contour with cut after merging: t = 0.053ms and t = 0.054ms.

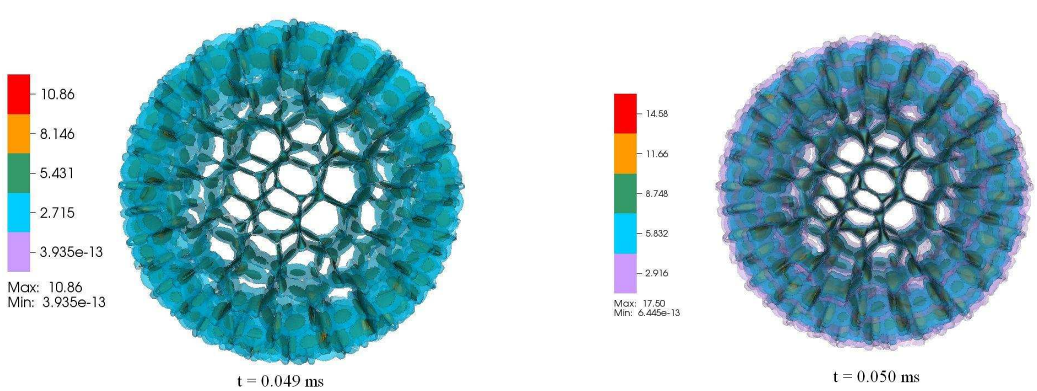

Figure 4.7: Pressure contour before merging: t = 0.049ms and t = 0.050ms

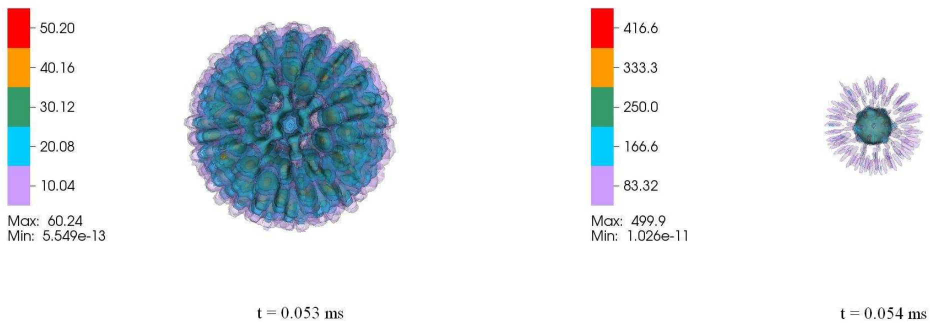

Figure 4.8: Pressure contour after merging: t = 0.053ms and t = 0.054ms.

velocity. The only change is the merging radius. Since the merging radius is changed, the number of jets is changed too. We will compare the merger of 125 and 625 jets corresponding to the merging radius of 50 and 100 cm correspondingly.

We performed 3 meter chamber simulations with $r_m = 50cm$ and $r_m = 100cm$ and the number of jets and their fadii before the merger as $N = 125, r_{jet} = 9cm$ and $N = 625, r_{jet} = 8cm$ correspondingly which the same $density\ limit = 3.6e - 06g/cc$.

Figure 4.9 shows the relation between the average Mach number and the radius.

At latyer stages of the liner implosion, 125 jets and 625 jets give almost the same Mach number, while at the early stages 125 jets show bigger average Mach number. The Mach numner reduction can be better described by comparing 1D and 3D liner as shown in Figure 4.10.

As the liner is compressing the target, the biggest density appears in the head of liner. We will change the measurement of liner radius. Originally we use the center position of each jet to calculate the liner radius. Now we use the density peak as liner radius. For the liner of 125 jets, density peak moves in about 15 cm in 0.001ms, while the peak of liner of 625 jets arrives the center. This is also predicted in Park's paper $\rho r^2 = constant$

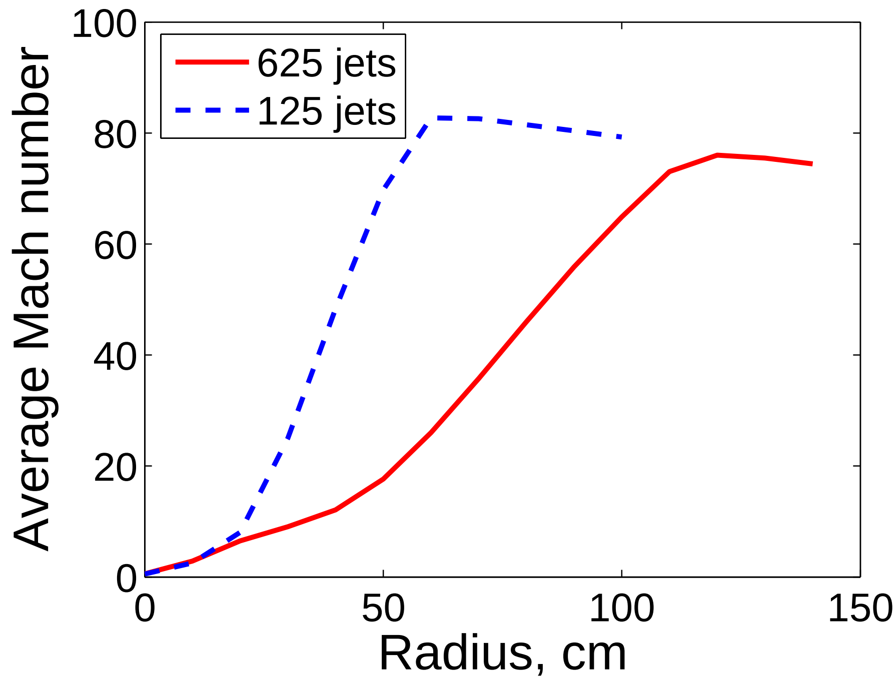

Figure 4.9: Mach number comparison for 125 jets and 625 jets

The pressure at merging time in perpendicular direction is shown in Figure (4.11). We still use the average pressure weighted by density to get rid of the effect of high vacuum.

$$\hat{P} = \frac{\int P * \rho}{\int \rho}$$

We choose $r = 27.5cm$ and $r = 12.5cm$ to compare 125 jets with 625 jets. We will use $\epsilon = 0.5$ to get a piece of liner $(r - \epsilon, r + \epsilon)$ and calculate the deviation in this piece. In fact the peak of 625 jets moves faster than the peak of 125 jets. After $r = 27.5cm$ at which 125 jets and 625 jets have the same peak position, the peak of 625 jets reach the $(0, 0, 0)$ when peak of 125 jets reach $r = 12.5cm$.

The deviation of the liner density and the pressure increase with number of jets. The range from the minimum density to the maximum density, the range from the

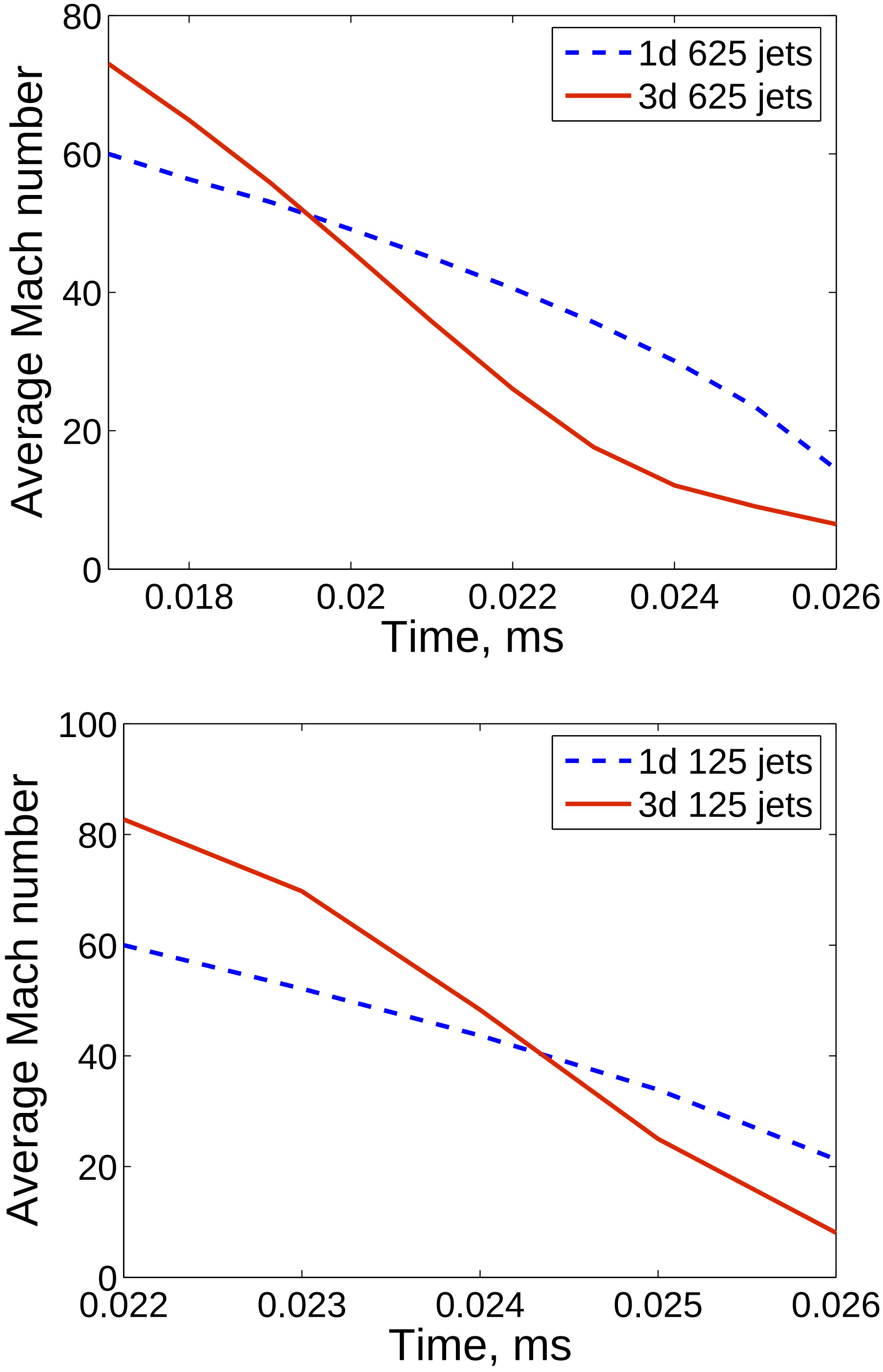

Figure 4.10: Top: 625 jets; bottom: 125 jets.

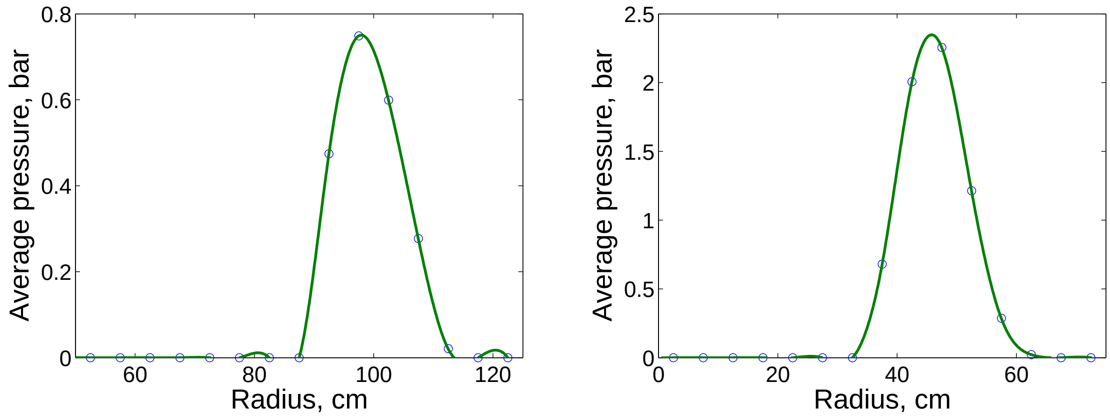

Figure 4.11: Left:625; right:125.

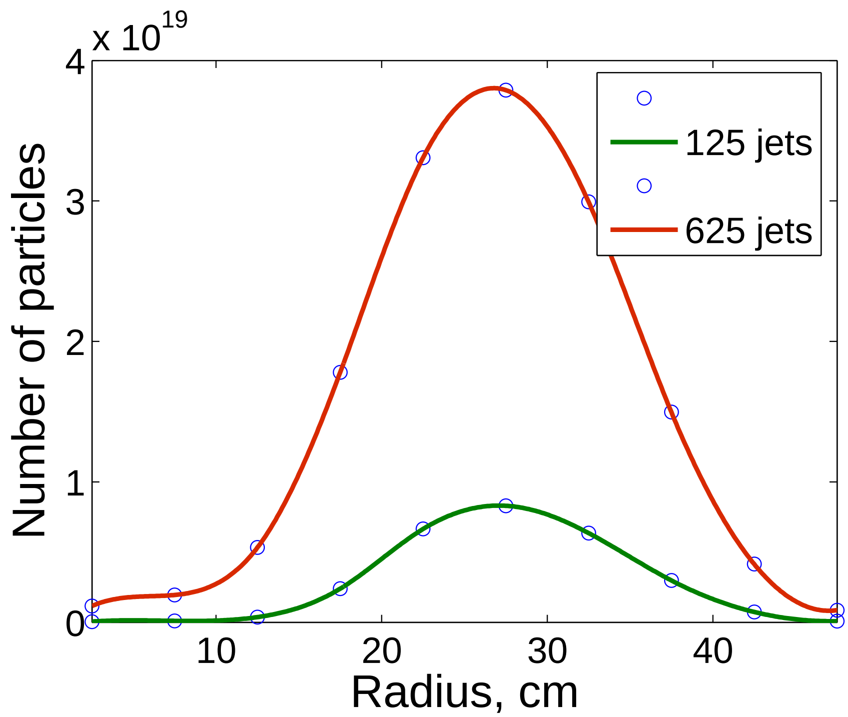

Table 4.1: Standard deviation for density

density	σ	max	relative σ
125 (r = 27.5)	1.99e-5	8.75e-5	0.5655
625 (r = 27.5)	6.52e-5	4.79e-4	0.4066
125 (r = 12.5)	3.84e-5	2.997e-4	0.4434
625 (r = 12.5)	4.93e-5	6.55e-4	0.1108

Table 4.2: Standard deviation for pressure

pressure	σ	max	relative σ
125 (r = 27.5)	40.36	153.4	1.0935
625 (r = 27.5)	59.21	509.7	0.4847
125 (r = 12.5)	129.89	1431	0.5362
625 (r = 12.5)	122.33	1249	0.1450

minimum pressure to the maximum pressure are also shown in the following table.

The relative deviation is defined by $relative\sigma = \frac{\sigma}{average}$. By comparing the relative deviation, we see that 625 jets generate more uniform liner that will generate less amount of the Rayleigh-Taylor instability in the target.

Spherical slice of 125 jet and 625 jets, density and pressure at r = 27.5 are shown in Figures (4.12)-(4.13).

Our numerical simulation results suggests that Mach number decreasing may not as much as Parks predicted because no strict oblique shock was observed during the jets merging process. In the future a fully three dimensional numerical simulation will answer the question about fusion gain and the target compression ratio. However development of new physics models is necessary to achieve better estimates of the fusion energy gain.

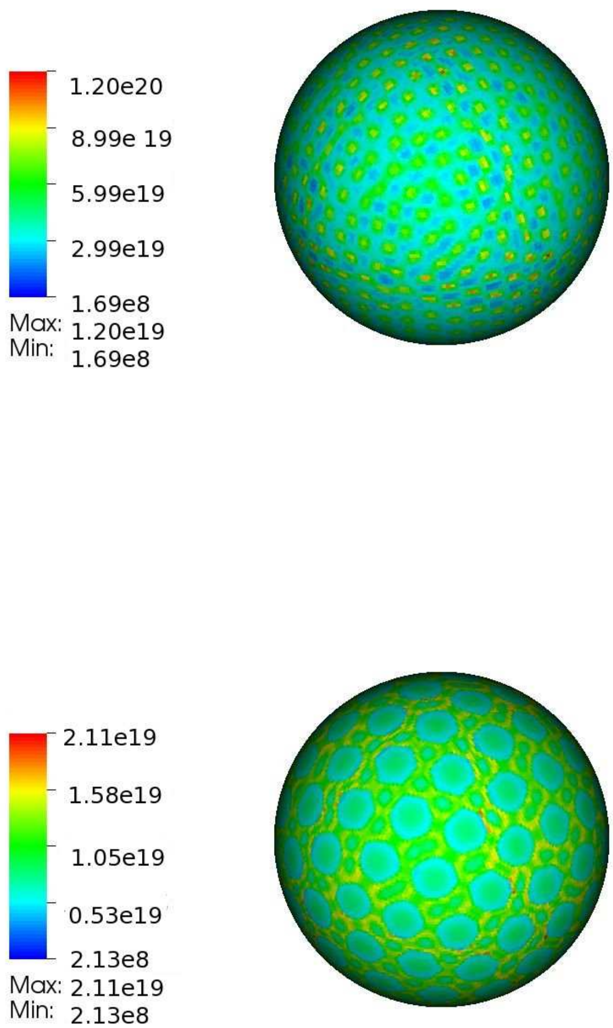

Figure 4.12: Left:625 jets; right:125 jets.

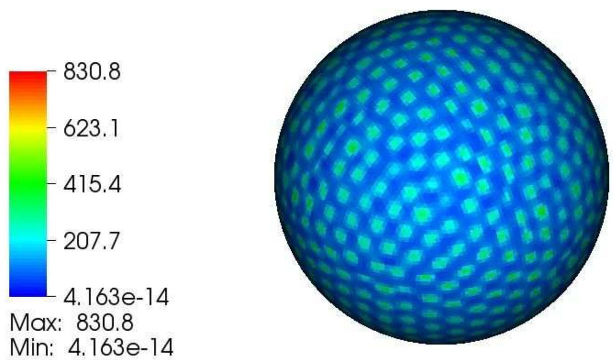

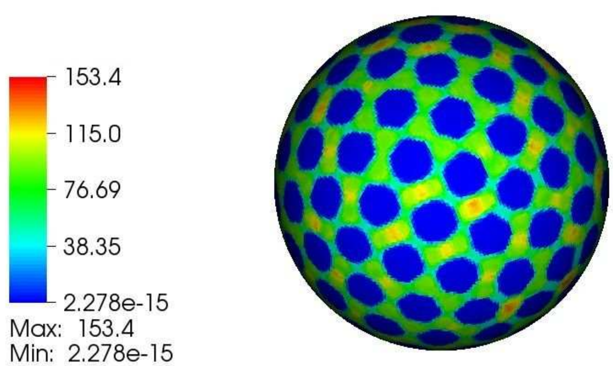

Figure 4.13: Left:625 jets; right:125 jets.

Chapter 5

4th order Solver for Maxwell Equation

5.1 Introduction

In this chapter, we focuse on the finite difference method for the Maxwell equations. Comparing to the finite element method, finite difference method is easy to implement and easy to couple with particle in cell technique which is important for many applications including PJMIF (plsma guns) and devices of particle accelerators. The idea of embedded boundary method will be adopted for geometrically complex domain.

5.1.1 FDTD method of Yee

The basic FDTD space grid and time-stepping algorithm trace back to a seminal 1966 paper by Kane Yee in IEEE Transactions on Antennas and Propagation [28]. Consider rectangular mesh shown in Figure 5.1. In the Yee FDTD scheme, the electric field is assigned to the edges of the mesh and the magnetic field is assigned to cell faces. In the second order discretization, the values of the electric and magnetic fields are constants on the cell edges and faces, correspondingly.

If we discrete the Maxwell equations far from the boundary, we obtain 6 equations

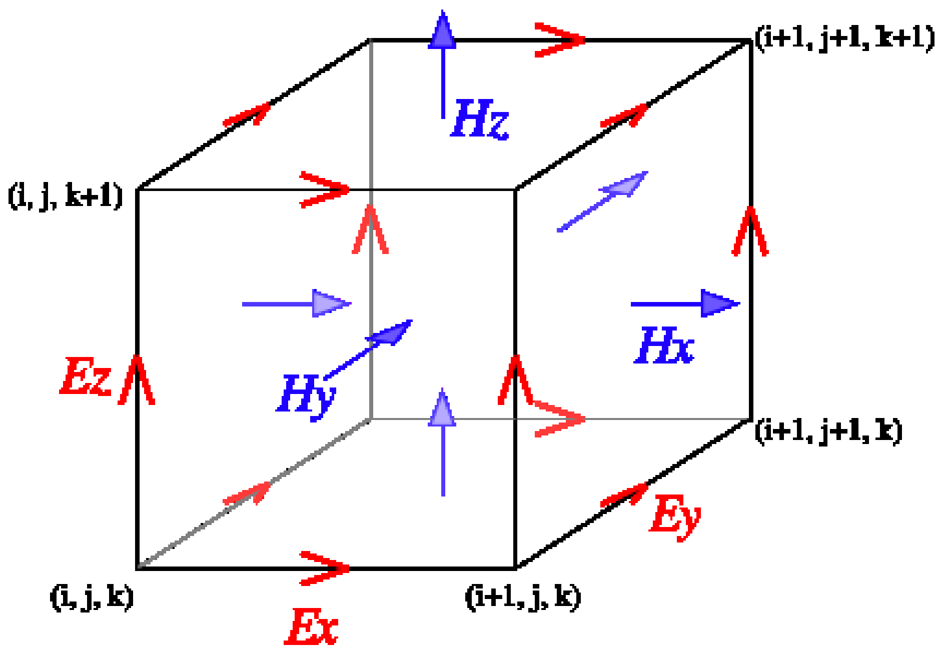

Figure 5.1: Yee cell

which depend on values located on only two-dimensional plane. The decoupling of three dimensional system of equations into a set of two-dimensional ones is one of the most important features of this method making it simple to implement and fast to compute. The discretized equations are as follows:

$$\frac{E^{n+1/2}_{x_{i,j,k}} - E^{n-1/2}_{x_{i,j,k}}}{dt} = \frac{1}{\epsilon}\left(\frac{H^n_{z_{i,j+1,k}} - H^n_{z_{i,j-1,k}}}{2dy} - \frac{H^n_{y_{i,j,k+1}} - H^n_{y_{i,j,k-1}}}{2dz}\right)$$

$$\frac{E^{n+1/2}_{y_{i,j,k}} - E^{n-1/2}_{y_{i,j,k}}}{dt} = \frac{1}{\epsilon}\left(\frac{H^n_{x_{i,j,k+1}} - H^n_{x_{i,j,k-1}}}{2dz} - \frac{H^n_{z_{i+1,j,k}} - H^n_{z_{i-1,j,k}}}{2dx}\right)$$

$$\frac{E^{n+1/2}_{z_{i,j,k}} - E^{n-1/2}_{z_{i,j,k}}}{dt} = \frac{1}{\epsilon}\left(\frac{H^n_{y_{i+1,j,k}} - H^n_{y_{i,j,k-1}}}{2dx} - \frac{H^n_{x_{i,j+1,k}} - H^n_{x_{i,j-1,k}}}{2dy}\right)$$

$$\frac{H^{n+1}_{x_{i,j,k}} - H^n_{x_{i,j,k}}}{dt} = -\frac{1}{\mu}\left(\frac{E^{n+1/2}_{z_{i,j+1,k}} - E^{n+1/2}_{z_{i,j-1,k}}}{2dy} - \frac{E^{n+1/2}_{y_{i,j,k+1}} - E^{n+1/2}_{y_{i,j,k-1}}}{2dz}\right)$$

$$\frac{H_{y_{i,j,k}}^{n+1}-H_{y_{i,j,k}}^{n}}{dt}=-\frac{1}{\mu}(\frac{E_{x_{i,j,k+1}}^{n+1/2}-E_{x_{i,j,k-1}}^{n+1/2}}{2dz}-\frac{E_{z_{i+1,j,k}}^{n+1/2}-E_{z_{i-1,j,k}}^{n+1/2}}{2dx})$$

$$\frac{H_{z_{i,j,k}}^{n+1}-H_{z_{i,j,k}}^{n}}{dt}=-\frac{1}{\mu}(\frac{E_{y_{i+1,j,k}}^{n+1/2}-E_{y_{i-1,j,k}}^{n+1/2}}{2dx}-\frac{E_{x_{i,j+1,k}}^{n+1/2}-E_{x_{i,j-1,k}}^{n+1/2}}{2dy}) \tag{5.1}$$

Furthermore, Yee proposed a leapfrog scheme for marching in time wherein the E-field and H-field updates are staggered so that E-field updates are conducted midway during each time-step between successive H-field updates, and conversely. This explicit time-stepping scheme avoids the need to solve simultaneous equations, and furthermore yields dissipation-free numerical wave propagation. The time step is limited by the standard CFL condition involving the computational grid size and the speed of light.

The disadvantage of FDTD method is also caused by the advantage of simplicity of dual grid. For some complex geometry domain, the staircase dual grid will introduce spurious waves and FDTD method becomes zeroth-order. However FDTD method is good for rectangular computational domains and shows second order in both space and time. The second order for space is coming from central difference and the second order for time is derived by leap frog scheme. Since E field are calculated at $n+\frac{1}{2}$ step, and H field are calculated at $n+1$ step. The dual grid is adopted in time too. Another view is one step forward time step and one step backward time step, and this easily give us the matrix formula for Maxwell differential equations.

Let us write the discrete formula for Maxwell equation. For example, the following is finite difference equation for E_x, and other components are same.

$$\frac{E_x^{n+\frac{1}{2}}(i,j,k)-E_x^{n-\frac{1}{2}}(i,j,k)}{dt}$$

$$=\frac{1}{\epsilon}*(\frac{H_z^n(i,j+1,k)-H_z^n(i,j-1,k)}{2dy}-\frac{H_y^n(i,j,k+1)-H_y^n(i,j,k-1)}{2dz}) \tag{5.2}$$

5.1.2 4th Order Explicit Method with Yoshida Time Stepping

In this section, we develop 4th order accurate discretization of the Maxwell system of equations using Yoshida's ideas of the combination of symplectic maps. For 4th order space discretization, we need to calculate $\frac{dH}{dx}$ and $\frac{dE}{dx}$.

In second order FDTD method,

$$\Delta_y(u_{i,j}) = \frac{1}{\Delta_y} * (u_{i,j+1/2} + u_{i,j-1/2}) \tag{5.3}$$

By Taylor series , we can obtain the 4th order central scheme

$$\Delta_y(u_{i,j}) = \frac{1}{\Delta_y} * (-1/24u_{i,j-3/2} + 9/8u_{i,j-1/2} + 9/8u_{i,j+1/2} + 1/24u_{i,j+3/2}) \tag{5.4}$$

If near the boundary, one-side stencil will be adopted.

Compact method will use smaller stencil, 3 points instead of 5 points, but need to solve linear system every time step [29].

$$A = \frac{1}{24}\begin{pmatrix} 26 & -5 & 4 & -1 & 0 & \dots & 0 \\ 1 & 22 & 1 & 0 & 0 & \dots & 0 \\ 0 & 1 & 22 & 1 & 0 & \dots & 0 \\ \vdots & \ddots & \ddots & \ddots & \ddots & \ddots & \vdots \\ 0 & 0 & \dots & 1 & 22 & 1 & 0 \\ 0 & 0 & \dots & 0 & 1 & 22 & 1 \\ 0 & 0 & \dots & -1 & 4 & -5 & 26 \end{pmatrix} \tag{5.5}$$

$$A\frac{\partial}{\partial y}\begin{pmatrix} u^{1/2} \\ u^{3/2} \\ \vdots \\ u^{(2n-1)/2} \end{pmatrix} = \frac{1}{\Delta y} * (\begin{pmatrix} u^{1} \\ u^{2} \\ \vdots \\ u^{n} \end{pmatrix} - \begin{pmatrix} u^{0} \\ u^{1} \\ \vdots \\ u^{n-1} \end{pmatrix}) \tag{5.6}$$

The most common method for 4th order time discretization is the 4th order Runge-Kutta scheme:

$$E_z^{n+1} = E_z^n + \frac{\Delta t}{6}(k_1 + 2k_2 + 2K_3 + k_4)$$

$$\begin{aligned} t^{n+1} &= t^n + \Delta t \\ k_1 &= \frac{\partial H_y^n}{\partial x} - \frac{\partial H_x^n}{\partial y} \\ k_2 &= \frac{\partial H_y^{n+1/2\Delta t}}{\partial x} - \frac{\partial H_x^{n+1/2\Delta t}}{\partial y} \\ k_3 &= \frac{\partial H_y^{\star}}{\partial x} - \frac{\partial H_x^{\star}}{\partial y} \\ k_4 &= \frac{\partial H_y^{n+\Delta t}}{\partial x} - \frac{\partial H_x^{n+\Delta t}}{\partial y} \end{aligned} \tag{5.7}$$

The disadvantage of the Runge-Kutta scheme is the loss of simplectic property due to the fact that the scheme was developed based on truncated Taylor series. Physically, the loss of symplecticity leads to the loss of energy conservation which can be critical for long-time simulations of high-frequency processes. For instance, non-simplectic methods can not be used for the modeling of long-time, multiple-turn dynamics of particles in accelerators: the loss of energy conservation due to numerical errors would lead to the deviation of trajectories of particles which eventually would fall on the accelerator chamber wall.

The second order leap-frog algorithm is symplectic. To preserve the symplecticity of the 4th order time stepping, we used the Yoshida approach. The main result due to Yoshida, as well as wide applicability of his approach, is described in [30]. Let M_{2n} is a symplectic mapping that is an approximate solution to the problem and is accurate to the order $2n$. Also suppose that M_{2n} has the following property

$$M_{2n}(t)M_{2n}(-t) = I,$$

where I is the identity mapping. Then the following mapping is symplectic and accurate through order $2n + 2$:

$$M_{2n+2}(t) = M_{2n}(Z_0 t)M_{2n}(Z_1 t)M_{2n}(Z_0 t), \tag{5.8}$$

where

$$Z_0 = \frac{1}{2 - 2^{1/(2n+1)}}, Z_1 = \frac{-2^{1/(2n+1)}}{2 - 2^{1/(2n+1)}}.$$

Therefore, the Yoshida method gives an algorithm of constructing higher order symplectic maps from lower order ones. In application to the time stepping problem for discrete Maxwell equations, the leap-frog scheme, which is a second-order symplectic map, can be used as a building bloc of a three step, 4th order symplectic scheme. The coefficients in the method of Yoshida are roots of an integral equation and may be not unique. Three leapfrog steps come with unique coefficients (1.351207191959657,-1.702414383919315,1.351207191959657). Piet Hut and Jun Makino called this positive-negative-positive process as dancing-cat scheme.

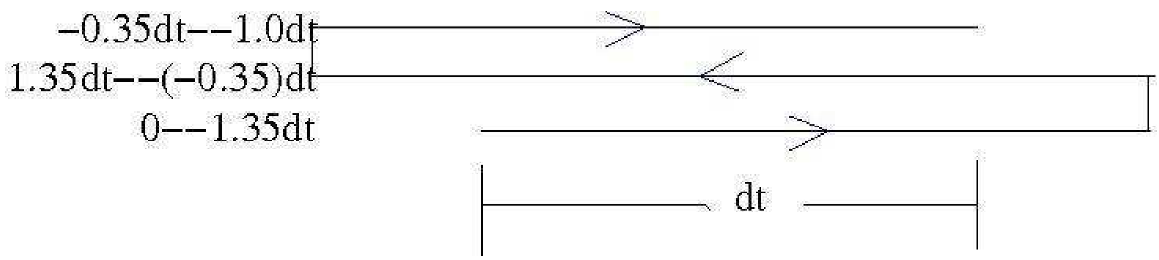

Figure 5.2: Yoshida 3 steps

5.1.3 Dey-Mittra Embedded Boundary Method

Dey and Mittra [4] developed a conformal (embedded boundary) FDTD method for the simulation of electromagnetic equations in geometrically complex domains. The schematic of the method is given in Figure 5.3. In the Dey-Mittra method, the undistorted cells are treated in the same way as in the standard Yee algorithm for both electrical and magnetical fields. For distorted cells, no special treatment is needed for the electric field. However the magnetical field will be calculated by using finite volume idea in an extended cell. It is assumed that H located in the center of the corresponding undistorted cell (the Cartesian cell obtained by removing the partial filling), irrespective of whether the location of the center is inside or outside the computational domain.

$$
\begin{aligned}
H_z^{n+1/2}(i,j,k) &= H_z^{n+1/2}(i,j,k) + \frac{\Delta t}{\mu * Area(i,j,k)} \\
&* \{E_x^n(i,j,k) * l_x(i,j,k) - E_x^n(i,j-1,k) * l_x(i,j-1,k)) \\
&- E_y^n(i,j,k) * l_y(i,j,k) - E_y^n(i-1,j,k) * l_y(i-1,j,k))\}
\end{aligned}
\tag{5.9}
$$

$$
\begin{aligned}
E_x^{n+1}(i,j,k) &= E_x^n(i,j,k) \\
&+ \frac{\Delta t}{\epsilon * \delta y} * \{H_z^{n+1/2}(i,j+1,k) - H_z^{n+1/2}(i,j,k)\}
\end{aligned}
$$

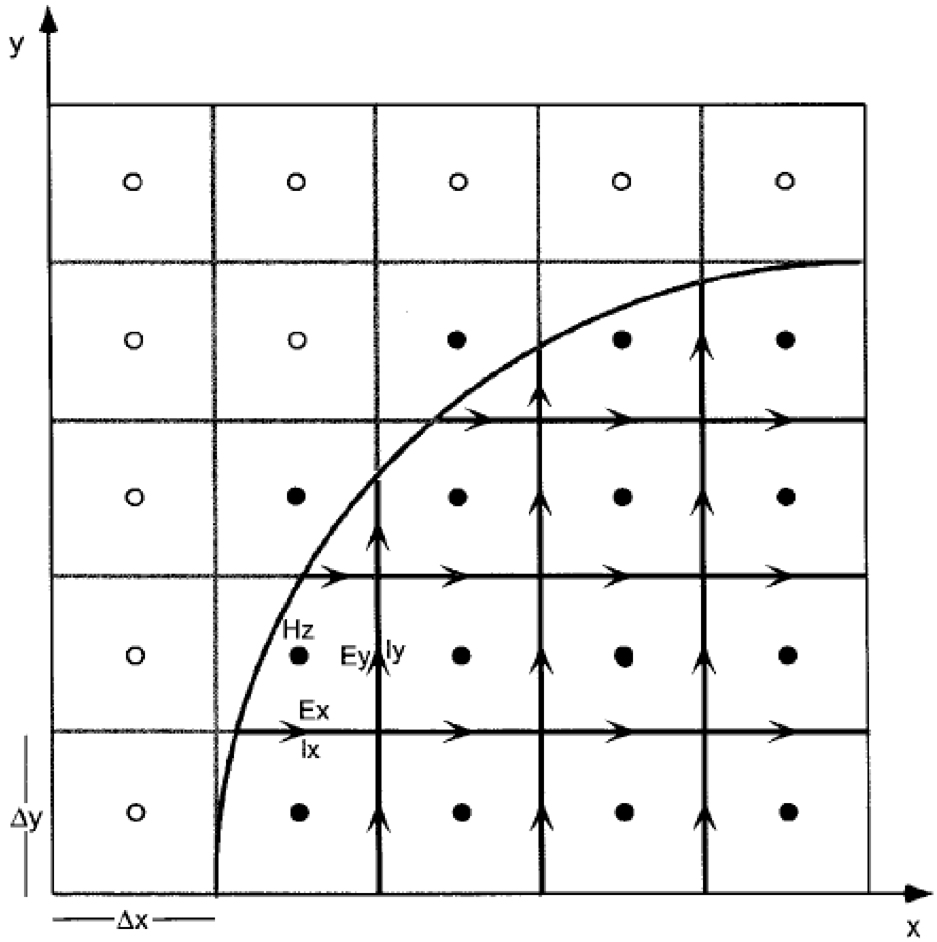

Figure 5.3: cut cell method

$$-\frac{\Delta t}{\epsilon * \delta z} * \{H_y^{n+1/2}(i+1,j,k) - H_y^{n+1/2}(i,j,k)\} \tag{5.10}$$

5.2 Numerical test problem set up

The exact solution for geometrically complex domain does not exist, so we have to use rectangular cavity as our numerical test problems. To obtain cut cells from rectangular cavity, a rotation will be conducted with a rotation matrix generated by Euler angle.

The analysis solution of TM (m,n,p) model is shown as following [3]. In the numerical test, we choose TM (1,1,0).

$$E_z(x,y,z) = E_0 sin(\frac{m\pi}{a}x) sin(\frac{n\pi}{b}y) cos(\frac{p\pi}{d}z)$$

$$E_x(x,y,z) = -\frac{1}{h^2}\frac{m\pi}{a}\frac{p\pi}{d}E_0 cos(\frac{m\pi}{a}x) sin(\frac{n\pi}{b}y) sin\frac{p\pi}{d}z)$$

$$E_y(x,y,z) = -\frac{1}{h^2}\frac{n\pi}{b}\frac{p\pi}{d}E_0 sin(\frac{m\pi}{a}x) cos(\frac{n\pi}{b}y) sin\frac{p\pi}{d}z)$$

$$H_x(x,y,z) = \frac{j\omega\epsilon}{h^2}\frac{n\pi}{b}E_0 sin(\frac{m\pi}{a}x) cos(\frac{n\pi}{b}y) cos\frac{p\pi}{d}z)$$

$$H_y(x,y,z) = -\frac{j\omega\epsilon}{h^2}\frac{m\pi}{a}E_0 cos(\frac{m\pi}{a}x) sin(\frac{n\pi}{b}y) cos\frac{p\pi}{d}z)$$

Here:$h^2 = (\frac{m\pi}{a})^2 + (\frac{n\pi}{b})^2$

We will use a rotation to get cut cell and then calculate the error by reverse rotation. The advantage is the exact solution is easier to obtain than other shape.

$$R^{-1} = R^T$$

$$R = \begin{bmatrix} \cos\alpha\cos\gamma - \cos\beta\sin\alpha\sin\gamma & -\cos\beta\cos\gamma\sin\alpha - \cos\alpha\sin\gamma & \sin\alpha\sin\beta \\ \cos\gamma\sin\alpha + \cos\alpha\cos\beta\sin\gamma & \cos\alpha\cos\beta\cos\gamma - \sin\alpha\sin\gamma & -\cos\alpha\sin\beta \\ \sin\beta\sin\gamma & \cos\gamma\sin\beta & \cos\beta \end{bmatrix} \tag{5.11}$$

The following table shows the numerical results. The order is a little worse than 2nd order because percentage of cut cells is too high, so the error from first order approximation dominate.

This numerical test uses CFL=0.5, Euler angle=PI/3.0,PI/4.0,PI/5.0. Here grid number is the total computational domain contain some outside cavity domain. Even

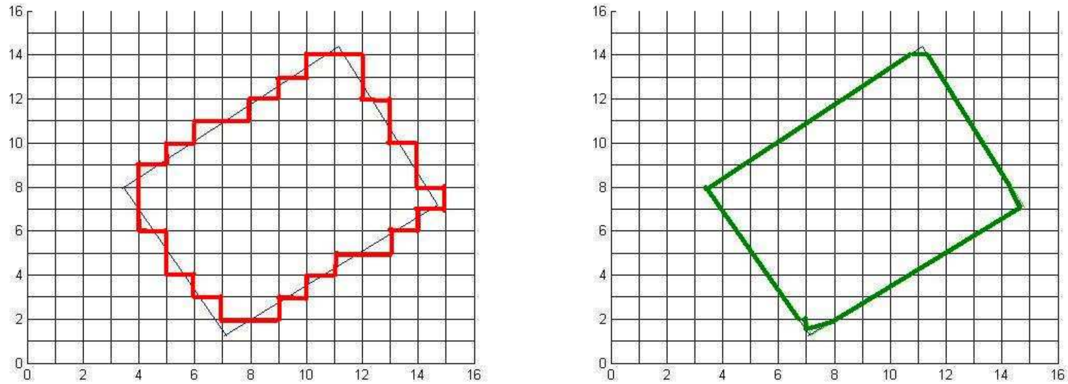

Figure 5.4: Left: stair case; right: cut cell case

Table 5.1: 2nd order numerical examination

grid	L_2 normal error	order
16*16*16	3.2e-2	NA
32*32*32	2.7e-2	1.25
64*64*64	1.8e-2	1.47
128*128*128	1.2e-	1.42

in 128^3 domain, cut cells percentage is greater than 0.05 which makes error bigger than theoretical analysis.

5.3 Simulation Results and Stability Analysis

In this section, we will show CFL condition and leading error term for 4th order center scheme in space and 4th order Yoshida scheme for time.[15]

5.3.1 Stability for General Hyperbolic Laws

For the stability analysis, it is sufficient to consider a linear system of hyperbolic laws.

$$\frac{\partial u}{\partial t} = \vec{A} \cdot \nabla u. \tag{5.12}$$

Here $u(x,t) = (u_1, u_2, ..., u_n)$, and $\vec{A}$ is a d-vector of $n \times n$ matrices. A finite difference solver is stable if and only if there is no unstable mode. To construct an unstable mode, let

$$u(x,0) = e^{i\vec{k}\cdot\vec{x}} u_0.$$

The spatial differentiation is approximated by certain finite difference. Under such approximation, spatial differentiation becomes a constant factor. For convenience we denote the factor by $i\vec{\alpha}$. For example, the central difference scheme gives

$$\frac{\partial u(\vec{x})}{\partial x_j} \doteq \frac{u(\vec{x} + \frac{\Delta x_j}{2}\vec{e}_j) - u(\vec{x} + \frac{\Delta x_j}{2}\vec{e}_j)}{\Delta x_j} = \frac{2i\sin(\frac{k_j \Delta x_j}{2})}{\Delta x_j} u(\vec{x}),$$

and so

$$\hat{\nabla} u = i\vec{\alpha} u = i \left(2 \sum_{j=1}^{d} \frac{\vec{e}_j}{\Delta x_j} \sin\theta_j \right) u. \tag{5.13}$$

where $\hat{\nabla}$ denotes the finite difference approximation of ∇, and $\theta_j = k_j \Delta x_j / 2$. For $|\vec{\theta}| \ll 1$, $\vec{\alpha} \approx \vec{k}$. For the 4th order central difference scheme,

$$\frac{\partial u(\vec{x})}{\partial x_j} \doteq \frac{-\frac{1}{24}u(\vec{x} + \frac{3\Delta x_j}{2}\vec{e}_j) + \frac{9}{8}u(\vec{x} + \frac{\Delta x_j}{2}\vec{e}_j) - \frac{9}{8}u(\vec{x} - \frac{\Delta x_j}{2}\vec{e}_j) + \frac{1}{24}u(\vec{x} - \frac{3\Delta x_j}{2}\vec{e}_j)}{\Delta x_j},$$

the corresponding $\vec{\alpha}$ is

$$\vec{\alpha} = 2\sum_{j=1}^{d} \frac{\vec{e}_j}{\Delta x_j} \left(\frac{9}{8}\sin\theta_j - \frac{1}{24}\sin(3\theta_j) \right) = 2\sum_{j=1}^{d} \frac{\vec{e}_j}{\Delta x_j} \left(\sin\theta_j + \frac{1}{6}\sin^3\theta_j \right), \tag{5.14}$$

with the same θ_j as defined before.

Given $\vec{\alpha}$, the solver becomes an ODE solver. Denote the propagation matrix of the solver from 0 to Δt by O, $i.e.\hat{u}(\Delta t) = Ou(0)$. The stability condition is that all eigenvalues of O for any $\vec{k}$, or equivalently, for any $\vec{\theta}$ have norms no larger than 1.

Now we specialize the stability analysis to symplectic solvers of the Maxwell

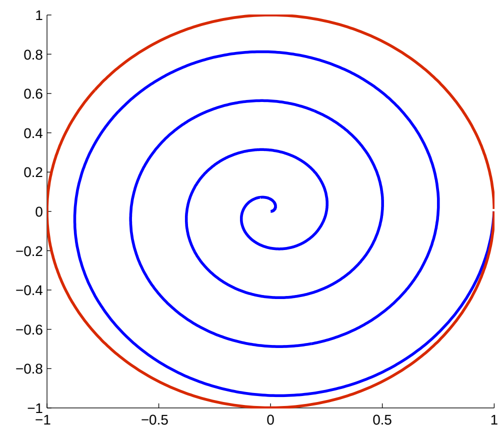

Figure 5.5: Eigenvalue for symplectics methods and non-symplectics methods

equations in the three dimensional vacuum space. Assuming $c = 1$,

$$\frac{\partial \vec{E}}{\partial t} = \nabla \times \vec{B}, \quad \frac{\partial \vec{B}}{\partial t} = -\nabla \times \vec{E}. \tag{5.15}$$

Define the propagation matrices O_t^E and O_t^B respectively by

$$O_t^E \begin{pmatrix} \vec{E} \\ \vec{B} \end{pmatrix} = \begin{pmatrix} \vec{E} + t\hat{\nabla} \times \vec{B} \\ \vec{B} \end{pmatrix}, \quad O_t^B \begin{pmatrix} \vec{E} \\ \vec{B} \end{pmatrix} = \begin{pmatrix} \vec{E} \\ \vec{B} - t\hat{\nabla} \times \vec{E} \end{pmatrix}.$$

A symplectic solver takes the form

$$O = O_{t_{2k}}^B O_{t_{2k-1}}^E \ldots O_{t_2}^B O_{t_1}^E, \tag{5.16}$$

in which

$$t_1 + t_3 + \ldots + t_{2k-1} = t_2 + t_4 + \ldots + t_{2k} = \Delta t, \tag{5.17}$$

with possible zero t_i's.

To do the stability analysis, replace $\hat{\nabla}$ by $i\vec{\alpha}$. Decompose $\vec{E}$ and $\vec{B}$ to components parallel to $\vec{\alpha}$ and perpendicular to $\vec{\alpha}$, $\vec{E} = \vec{E}_{||} + \vec{E}_{\perp}$, $\vec{B} = \vec{B}_{||} + \vec{B}_{\perp}$. Since O_t^E and O_t^B don't change $\vec{E}_{||}$ and $\vec{B}_{||}$, except for the uninteresting eigenvalue of 1, we can assume $\vec{E}$ and $\vec{B}$ are perpendicular to $\vec{\alpha}$. Denote $i(\vec{\alpha}/\alpha) \times \vec{B}$ by $\vec{D}$ (where $\alpha = |\vec{\alpha}|$), the propagation matrices of O_t^E and O_t^B can be rewritten as

$$O_t^E \begin{pmatrix} \vec{E} \\ \vec{D} \end{pmatrix} = \begin{pmatrix} \vec{E} + t\alpha\vec{D} \\ \vec{D} \end{pmatrix}, \quad O_t^B \begin{pmatrix} \vec{E} \\ \vec{D} \end{pmatrix} = \begin{pmatrix} \vec{E} \\ \vec{D} - t\alpha\vec{E} \end{pmatrix}. \tag{5.18}$$

From the equations above it is clear that with given $\vec{\alpha}$, the spectrum of O for the Maxwell equations is the same (except possibly the uninteresting eigenvalue of 1) as the spectrum of the same solver O in Eq. (5.16) applied to the ODE,

$$\frac{\mathrm{d}E}{\mathrm{d}t} = \alpha D, \quad \frac{\mathrm{d}D}{\mathrm{d}t} = -\alpha E. \tag{5.19}$$

Here the action of O_t^E and O_t^B on (E, D) are given by Eq. (5.18) with the vectors replaced by corresponding scalars. O has determinant 1 because all O_t^E and O_t^B in Eq. (5.18) have determinant 1. The 2×2 matrix O with determinant 1 has eigenvalues with norm no larger than 1 if and only if

$$|\mathrm{Tr}(O)| \leq 2$$

.

Denote O by

$$O = \begin{pmatrix} O_{11} & O_{12} \\ O_{21} & O_{22} \end{pmatrix}.$$

Its explicit form is

$$
\begin{aligned}
O_{11} &= 1-\alpha^2 \sum_{\substack{i_1>i_2 \\ \text{alt. parity, } \mathrm{i}_1 \text{ odd}}} t_{i_1}t_{i_2} + \alpha^4 \sum_{\substack{i_1>i_2>i_3>i_4 \\ \text{alt. parity, } \mathrm{i}_1 \text{ odd}}} t_{i_1}t_{i_2}t_{i_3}t_{i_4} - \ldots \\
O_{12} &= \alpha \sum_{i_1 \text{ odd}} t_{i_1} - \alpha^3 \sum_{\substack{i_1>i_2>i_3 \\ \text{alt. parity, } \mathrm{i}_1 \text{ odd}}} t_{i_1}t_{i_2}t_{i_3} + \ldots \\
O_{21} &= -\alpha \sum_{i_1 \text{ even}} t_{i_1} + \alpha^3 \sum_{\substack{i_1>i_2>i_3 \\ \text{alt. parity, } \mathrm{i}_1 \text{ even}}} t_{i_1}t_{i_2}t_{i_3} - \ldots \\
O_{22} &= 1-\alpha^2 \sum_{\substack{i_1>i_2 \\ \text{alt. parity, } \mathrm{i}_1 \text{ even}}} t_{i_1}t_{i_2} + \alpha^4 \sum_{\substack{i_1>i_2>i_3>i_4 \\ \text{alt. parity, } \mathrm{i}_1 \text{ even}}} t_{i_1}t_{i_2}t_{i_3}t_{i_4} - \ldots
\end{aligned}
$$

All subscripts of t are within the range from 1 to $2k$, and each equation has no more than $k+1$ terms. Adding up O_{11} and O_{22},

$$
\begin{aligned}
\mathrm{Tr}(O) &= 2-\alpha^2 \sum_{\substack{i_1>i_2 \\ \text{alt. parity}}} t_{i_1}t_{i_2} + \alpha^4 \sum_{\substack{i_1>i_2>i_3>i_4 \\ \text{alt. parity}}} t_{i_1}t_{i_2}t_{i_3}t_{i_4} - \ldots \\
&= 2-\alpha^2\Delta t^2 + \alpha^4 \sum_{\substack{i_1>i_2>i_3>i_4 \\ \text{alt. parity}}} t_{i_1}t_{i_2}t_{i_3}t_{i_4} - \ldots . \qquad (5.20)
\end{aligned}
$$

Equation (5.17) has been used in the derivation of the coefficient of α^2.

The actual calculation of $\mathrm{Tr}(O)$ can be simplified if we know the order of the scheme. Suppose the scheme is of order at least $2m$ in time, then we know $\mathrm{Tr}(O)$ is accurate at least up to Δt^{2m}. The solution to Eq. (5.19) has the exact propagation matrix,

$$O_{ex} = \begin{pmatrix} \cos\alpha\Delta t & \sin\alpha\Delta t \\ -\sin\alpha\Delta t & \cos\alpha\Delta t \end{pmatrix},$$

which gives

$$\mathrm{Tr}(O_{ex}) = 2\cos\alpha\Delta t = 2 - \alpha^2\Delta t^2 + \frac{2}{4!}\alpha^4\Delta t^4 - \ldots. \tag{5.21}$$

For the purpose of stability analysis, we can assume that the scheme has even number of nonzero sub steps. To see that, assume $t_{2k} = 0$, then $Tr(O) = Tr(O')$, where

$$O' = O^B_{t_{2k-2}} O^E_{t_{2k-3}} \ldots O^B_{t_2} O^E_{t_1} O^E_{t_{2k-1}} = O^B_{t_{2k-2}} O^E_{t_{2k-3}} \ldots O^B_{t_2} O^E_{t_1+t_{2k-1}}. \tag{5.22}$$

The leap-frog scheme has nonzero sub steps

$$t_1 = t_3 = \frac{\Delta t}{2}, \quad t_2 = \Delta t, \tag{5.23}$$

or equivalently by Eq. (5.22), $t_1 = t_2 = \Delta t$. The stability condition is

$$|\mathrm{Tr}(O)| = |2 - \alpha^2\Delta t^2| \le 2,$$

or equivalently, $|\alpha\Delta t| \le 2$. For the 2nd order spatial central difference scheme, using Eq. (5.13) we arrive at the CFL condition

$$\Delta t \max_{\vec{\theta}} |\tfrac{1}{2}\vec{\alpha}(\vec{\theta})| = \Delta t \sqrt{\sum_{j=1}^{3} (\Delta x_j)^{-2}} \le 1.$$

For the 4th order spatial central difference scheme, using Eq. (5.14) we arrive at the CFL condition

$$\Delta t \max_{\vec{\theta}} |\tfrac{1}{2}\vec{\alpha}(\vec{\theta})| = \frac{7}{6}\Delta t \sqrt{\sum_{j=1}^{3}(\Delta x_j)^{-2}} \leq 1.$$

The 4th order symplectic scheme has nonzero sub steps

$$t_1 = t_7 = \frac{1}{2(1+a)}\Delta t, \quad t_3 = t_5 = \frac{a}{2(1+a)}\Delta t, \quad t_2 = t_6 = \frac{1}{1+a}\Delta t, \quad t_4 = \frac{a-1}{1+a}\Delta t, \tag{5.24}$$

where $a = 1 - \sqrt[3]{2}$. In terms of stability, it is more convenient to use the equivalent scheme with

$$t_1 = \frac{1}{1+a}\Delta t, \quad t_3 = t_5 = \frac{a}{2(1+a)}\Delta t, \quad t_2 = t_6 = \frac{1}{1+a}\Delta t, \quad t_4 = \frac{a-1}{1+a}\Delta t.$$

Since the scheme is 4th order in time, the coefficient of α^4 in Eq. (5.20) is the same as in Eq. (5.21). Therefore the stability condition is

$$|2-\alpha^2\Delta t^2+\frac{1}{12}\alpha^4\Delta t^4-\alpha^6 t_1t_2t_3t_4t_5t_6| = |2-\alpha^2\Delta t^2+\frac{1}{12}\alpha^4\Delta t^4-\frac{a^2(a-1)}{4(1+a)^6}\alpha^6\Delta t^6| \leq 2.$$

Substituting in the value of a, one can verify that the stability condition is

$$(\alpha\Delta t)^2 \leq 12(1-1/\sqrt[3]{2}).$$

Similarly, for the 2nd order spatial central difference scheme, the CFL condition is

$$\Delta t \max_{\vec{\theta}} |\tfrac{1}{2}\vec{\alpha}(\vec{\theta})| = \Delta t \sqrt{\sum_{j=1}^{3}(\Delta x_j)^{-2}} \leq \sqrt{3(1-1/\sqrt[3]{2})} \approx 0.7867.$$

For the 4th order spatial central difference scheme, the CFL condition is stricter by a factor of 6/7.

5.3.2 Error Analysis for the Maxwell Equations

For general hyperbolic conservation laws as in Eq. (5.12), the error at time t, denoted by $\Delta u(t)$, is

$$\Delta u(t) = \frac{1}{\Delta t}\int_0^t O_{ex}(\tau \rightarrow t)\delta u(\tau)d\tau, \tag{5.25}$$

where $\delta u(\tau)$ is the error introduced by the finite difference solver at time τ, and $O_{ex}(\tau \rightarrow t)$ is the propagation matrix from τ to t. For constant coefficient matrix A, $O_{ex}(\tau \rightarrow t)$ is a function of $t-\tau$ whose analytic form depends on the properties of $\delta u(\tau)$.

For the Maxwell equations given in Eq. (5.15), $\delta\vec{E}$ and $\delta\vec{B}$ consist of contributions from temporal and spatial discretizations.

$$\delta\vec{E} = k_E^n \partial_t^n E + \Delta t(\delta\nabla \times \vec{B}), \quad \delta\vec{B} = k_B^n \partial_t^n B - \Delta t(\delta\nabla \times \vec{E}), \tag{5.26}$$

where n is the leading order of the temporal error, and $\delta\nabla$ is the error of the gradient operator in the spatial central difference scheme. For the 2nd leap frog temporal scheme, $n = 3$ and

$$k_E^3 = \sum_{\substack{i_1 > i_2 > i_3 \\ \text{alt. parity, } \mathrm{i}_1 \text{ odd}}} t_{i_1} t_{i_2} t_{i_3} - \frac{(\Delta t)^3}{6}, \quad k_B^3 = \sum_{\substack{i_1 > i_2 > i_3 \\ \text{alt. parity, } \mathrm{i}_1 \text{ even}}} t_{i_1} t_{i_2} t_{i_3} - \frac{(\Delta t)^3}{6}, \tag{5.27}$$

with t_i's given in Eq. (5.23). For the 4th symplectic temporal scheme, $n = 5$ and

$$k_E^5 = \sum_{\substack{i_1 > \ldots > i_5 \\ \text{alt. parity, i}_1 \text{ odd}}} t_{i_1} t_{i_2} t_{i_3} t_{i_4} t_{i_5} - \frac{(\Delta t)^5}{120}, \quad k_B^5 = \sum_{\substack{i_1 > \ldots > i_5 \\ \text{alt. parity, i}_1 \text{ even}}} t_{i_1} t_{i_2} t_{i_3} t_{i_4} t_{i_5} - \frac{(\Delta t)^5}{120}, \tag{5.28}$$

with t_i's given in Eq. (5.24). For the 2nd order spatial central difference,

$$\delta\nabla = \sum_{j=1}^{3} \frac{1}{24} \vec{e}_j (\Delta x_j)^2 \partial_{x_j}^3. \tag{5.29}$$

For the 4th order spatial central difference

$$\delta\nabla = -\sum_{j=1}^{3} \frac{3}{640} \vec{e}_j (\Delta x_j)^4 \partial_{x_j}^5. \tag{5.30}$$

Now we derive the propagation of the error for monochromatic waves. For a monochromatic wave with the following form,

$$\vec{E}(t) = \vec{E}_0 e^{-i\omega t}, \quad \vec{B}(t) = \vec{B}_0 e^{-i\omega t}, \tag{5.31}$$

it can be verified that $\delta\vec{E}$ and $\delta\vec{B}$ satisfy the following conditions if they are substituted into $\vec{E}_i$ and $\vec{B}_i$ respectively,

$$\nabla^2 \vec{E}_i = -\omega^2 \vec{E}_i, \quad \nabla^2 \vec{B}_i = -\omega^2 \vec{B}_i. \tag{5.32}$$

With such initial conditions, the propagated fields after time t are

$$\vec{E}(t) = (\vec{E}_i + \frac{\nabla(\nabla\cdot\vec{E}_i)}{\omega^2})\cos\omega t - \frac{\nabla(\nabla\cdot\vec{E}_i)}{\omega^2} + \frac{\sin\omega t}{\omega}\nabla\times\vec{B}_i \tag{5.33}$$

$$\vec{B}(t) = (\vec{B}_i + \frac{\nabla(\nabla\cdot\vec{B}_i)}{\omega^2})\cos\omega t - \frac{\nabla(\nabla\cdot\vec{B}_i)}{\omega^2} - \frac{\sin\omega t}{\omega}\nabla\times\vec{E}_i \tag{5.34}$$

Be aware that $\delta\vec{E}$ and $\delta\vec{B}$ are not divergence free as $\vec{E}$ and $\vec{B}$.

Now we can apply Eq. (5.25) to find the accumulated error of $\vec{E}$ and $\vec{B}$ at time t. Here we are interested in the error for large t, *i.e.*,

$$\omega t \gg 1.$$

For large t, the dominant error is from the components in the propagated errors that add up coherently. More specifically, substituting Eq. (5.33) into Eq. (5.25), we have

$$\begin{aligned}
\Delta\vec{E}(t) &= \int_0^t \frac{d\tau}{\Delta t}[(\delta\vec{E}(\tau) + \frac{\nabla(\nabla\cdot\delta\vec{E}(\tau))}{\omega^2})\cos\omega(t-\tau) - \frac{\nabla(\nabla\cdot\delta\vec{E}(\tau))}{\omega^2} + \frac{\sin\omega(t-\tau)}{\omega}\nabla\times\delta\vec{B}(\tau)] \\
&\doteq \int_0^t \frac{d\tau}{\Delta t}[\tfrac{1}{2}(\delta\vec{E}(t) + \frac{\nabla(\nabla\cdot\delta\vec{E}(t))}{\omega^2}) + \frac{i}{2}\frac{\nabla\times\delta\vec{B}(t)}{\omega}] \\
&= \frac{t}{2\Delta t}[\delta\vec{E}(t) + \frac{\nabla(\nabla\cdot\delta\vec{E}(t))}{\omega^2} + i\frac{\nabla\times\delta\vec{B}(t)}{\omega}]
\end{aligned} \tag{5.35}$$

Substituting Eq. (5.26) into Eq. (5.35), and using Eq. (5.31) along with the condition $\nabla\cdot\vec{E} = 0$ in the vacuum, we have

$$\begin{aligned}
\Delta\vec{E} &= \frac{t}{2\Delta t}\{(k_E^n + k_B^n)\partial_t^n\vec{E} - \frac{i\Delta t}{\omega}[\delta\nabla\times(\nabla\times\vec{E}) - \nabla(\delta\nabla\cdot\vec{E}) + \nabla\times(\delta\nabla\times\vec{E})]\} \\
&= \frac{t}{2\Delta t}\{(k_E^n + k_B^n)\partial_t^n + \frac{2i\Delta t}{\omega}(\nabla\cdot\delta\nabla)\}\vec{E}.
\end{aligned} \tag{5.36}$$

Similarly, substituting Eqs. (5.34) and (5.26) into Eq. (5.25), we get the error in the magnetic field,

$$\begin{aligned}\Delta\vec{B}(t) &= \frac{t}{2\Delta t}[\delta\vec{B}(t) + \frac{\nabla(\nabla\cdot\delta\vec{B}(t))}{\omega^2} - i\frac{\nabla\times\delta\vec{E}(t)}{\omega}] \\ &= \frac{t}{2\Delta t}\{(k_E^n + k_B^n)\partial_t^n + \frac{2i\Delta t}{\omega}(\nabla\cdot\delta\nabla)\}\vec{B}. \qquad (5.37)\end{aligned}$$

Note that Eqs. (5.36) and (5.37) are the action of the same operator on $\vec{E}$ and $\vec{B}$ respectively. For arbitrary electromagnetic waves, the error need to be integrated over the spectrum. Assuming $\omega t \gg 1$ over the entire spectrum of the wave, the error in the electric field is

$$\Delta\vec{E}(t) = \frac{t}{2\Delta t}(k_E^n + k_B^n)\partial_t^n\vec{E}(t) + \nabla\cdot\delta\nabla\int_0^t \vec{E}(\tau)\tau d\tau.$$

The same formula applies to the magnetic field with all $\vec{E}$'s replaced by $\vec{B}$'s.

Substituting Eqs. (5.27) and (5.29) along with $n = 3$ into Eq. (5.36), we have

$$\Delta\vec{E}(t) = \frac{it}{24\omega}[\sum_{j=1}^{3}(\Delta x_j)^2\partial_{x_j}^4 - (\Delta t)^2\omega^4]\vec{E}(t).$$

The same formula applies to $\Delta\vec{B}(t)$ with $\vec{E}(t)$ replaced by $\vec{B}(t)$. It has a $\pi/2$ phase difference from the actual field.

For a single mode wave, $\partial_{x_j}^2\vec{E} = -k_j^2\vec{E}$. The error is proportional to $\sum_{j=1}^{3}(\Delta x_j)^2 k_j^4 - (\Delta t)^2\omega^4$, which is minimized when Δt satisfies the maximum CFL condition,

$$\Delta t^{-2} = \sum_{j=1}^{3}(\Delta x_j)^{-2}.$$

Since the average L_2 error of the field is the sum of the L_2 error of single mode waves, the total error is also minimized when Δt satisfies the maximum CFL condition.

Substituting Eqs. (5.28) and (5.30) along with $n = 5$ into Eq. (5.36), we have

$$\begin{aligned}\Delta\vec{E}(t) &= \frac{-it}{2\omega}[\frac{3}{320}\sum_{j=1}^{3}(\Delta x_j)^4\partial_{x_j}^6 - (\Delta t)^4\omega^6(\frac{1-2a}{24(a+1)^2} + \frac{1}{60})]\vec{E}(t). \\ &\approx \frac{-3it}{640\omega}[\sum_{j=1}^{3}(\Delta x_j)^4\partial_{x_j}^6 - 14.11(\Delta t)^4\omega^6]\vec{E}(t).\end{aligned}$$

In the formula $a = 1 - \sqrt[3]{2}$. The average L_2 error of the field is smaller for a smaller Δt.

5.3.3 Comparison with Runge-Kutta

Similar to the analysis for symplectic schemes, we can derive the CFL condition and leading order error terms for Runge-Kutta schemes applied to the Maxwell equations. The stability condition of the PDE solver reduces to the ODE solver for Eq. (5.19) as before. The discretized propagator for the 2nd order Runge-Kutta scheme is

$$O = \begin{pmatrix} 1 - \frac{(\alpha\Delta t)^2}{2} & \alpha\Delta t \\ -\alpha\Delta t & 1 - \frac{(\alpha\Delta t)^2}{2} \end{pmatrix}.$$

Unlike symplectic schemes, the determinant of the matrix above is not 1. It's well known that the central difference scheme is unstable, and the 2nd order Runge-Kutta scheme based on spatial central difference is also unstable because

$$\det(O) = 1 + \frac{(\alpha\Delta t)^4}{4} > 1.$$

However, the 4th order Runge-Kutta scheme based on spatial central difference is conditionally stable. Indeed,

$$O = \begin{pmatrix} 1 - \frac{(\alpha\Delta t)^2}{2} + \frac{(\alpha\Delta t)^4}{24} & \alpha\Delta t - \frac{(\alpha\Delta t)^3}{6} \\ -\alpha\Delta t + \frac{(\alpha\Delta t)^3}{6} & 1 - \frac{(\alpha\Delta t)^2}{2} + \frac{(\alpha\Delta t)^4}{24} \end{pmatrix}, \tag{5.38}$$

and

$$\det(O) = 1 - \frac{(\alpha\Delta t)^6}{72} + \frac{(\alpha\Delta t)^8}{576} \leq 1 \qquad \text{for} \quad |\alpha\Delta \mathrm{t}| \leq 2\sqrt{2}.$$

So the CFL condition with the 4th order spatial central difference scheme is

$$\Delta t \max_{\vec{\theta}} |\tfrac{1}{2}\vec{\alpha}(\vec{\theta})| = \frac{7}{6}\Delta t \sqrt{\sum_{j=1}^{3}(\Delta x_j)^{-2}} \leq \sqrt{2}.$$

It is about 1.8 times less stringent than the CFL condition for the 4th order symplectic scheme. Similar analysis leads to the following dominant error in the electric field for the 4th order Runge-Kutta method with the 4th order spatial central difference scheme,

$$\Delta\vec{E}(t) = \frac{-3it}{640\omega}[\sum_{j=1}^{3}(\Delta x_j)^4 \partial_{x_j}^6 - \frac{16}{9}(\Delta t)^4\omega^6]\vec{E}(t).$$

It is noted that the 4th order Runge-Kutta method and the 4th order symplectic scheme based on the 4th order spatial central difference have the same order of accuracy in space and time, therefore they also conserve the total field energy up to the same order.

However, Runge-Kutta method has an significant deficiency. So far we have been discussing the stability and error of numerical schemes in the limit that $\Delta t \to 0$ with t fixed. Now we consider the stability from another point of view, *i.e.*, $t \to \infty$ with Δt fixed. Due to the symplectic structure of the Maxwell equations, $\vec{E}$ and $\vec{B}$ neither diverge to ∞ nor converge to 0 as time increases. A stable numerical solver should have the same property, but Runge-Kutta method does not have it. Since the eigenvalues of the propagator O in Eq. (5.38) has norm less than 1 for a stable scheme, for a given mode the wave at late time t is proportional to

$$\left(1 - \frac{(\alpha\Delta t)^6}{72} + \frac{(\alpha\Delta t)^8}{576}\right)^{\frac{t}{2\Delta t}} \approx \exp(-\frac{(\alpha\Delta t)^5}{144}\alpha t) \approx \exp(-\frac{(\omega\Delta t)^5}{144}\omega t), \tag{5.39}$$

which decreases exponentially in time. Here we assume that $\omega\Delta t = |\vec{k}|\Delta t \ll 1$. For a fixed Δt, the exponent in Eq. (5.39) can have a large negative value for large t, which makes the field converge to 0 undesirably. On the other hand, if we only care about the field propagation in finite time such that the exponent in Eq. (5.39) is always much less 1, Runge-Kutta scheme can still be used. It is noted that the undesirable convergence happens later in time for a higher order Runge-Kutta scheme. In contrast, the outcome of symplectic schemes neither increases nor decreases exponentially because the eigenvalues of their propagators all have norm 1.

Besides the long time stability, symplectic schemes requires less memory space than Runge-Kutta schemes. Since the symplectic scheme updates $\vec{E}$ and $\vec{B}$ alternatively, it only need the space for a set of $\vec{E}$ and $\vec{B}$ distributions. Runge-Kutta method need extra space to save the approximate temporal derivatives, *e.g.*, the total space needed for the 4th order scheme is 3 times of that for symplectic schemes.

For 4th order methods, the symplectic scheme has fewer sub steps than the Runge-Kutta scheme. Combining the last sub step and the first sub step of the next time step, the 4th order symplectic scheme has only 6 sub steps per step, while the 4th order Runge-Kutta method has 8 sub steps per step that calculate the temporal derivatives of the fields. However, the conclusion may not apply to higher order schemes. For examples, the 6th order symplectic scheme given by Yoshida[30] has 14 sub steps, while the 6th order Runge-Kutta scheme has only 12 sub steps.

Table 5.2: 4th order symplectic vs 4th order Runge-Kutta

	4th order Yoshida scheme	4th order Runge-Kutta scheme
memory space	2	6
CFL condition	0.7867	1.4142
Fix t, operation time	1.2622	1

Table 5.3: 4th order numerical examination

grid	L_2 normal error	order
16*16*16	1.44e-4	NA
32*32*32	6.96e-5	4.15
64*64*64	3.25e-6	4.19
128*128*128	1.63e-7	4.11

since we combine the first substep in t_{n+1} of Yoshida with the last substep in t_n, total operation time for Yoshida becomes 6*3*11. The total operation time for Runge-kutta is 6*(3*11+14). The step 1 to step 3 for Runge-Kutta are same as first order time forward while step 4 for Runge-Kutta need weighted sum. so total operation time ratio is determined by

$$\frac{Yoshida}{Runge-Kutta} = \frac{6*3*11/0.7867}{6*(3*11+14)/1.4142} = 1.2622$$

For regular grid, numerical order is verified as the following tables. CFL=0.5, Euler angle=0,0,0.

5.4 4th order Embedded Boundary Discretization

We notice that there is a "hidden" mapping between the point value and the average value in the 2nd order embedded boundary method. The mapping is hidden a 2nd order finite difference scheme is equivalent to a 2nd order finite volume scheme. E and H in FDTD scheme both represent point values, but in the 2nd order Embedded boundary method, H represents average value. This is because in the 2nd order finite

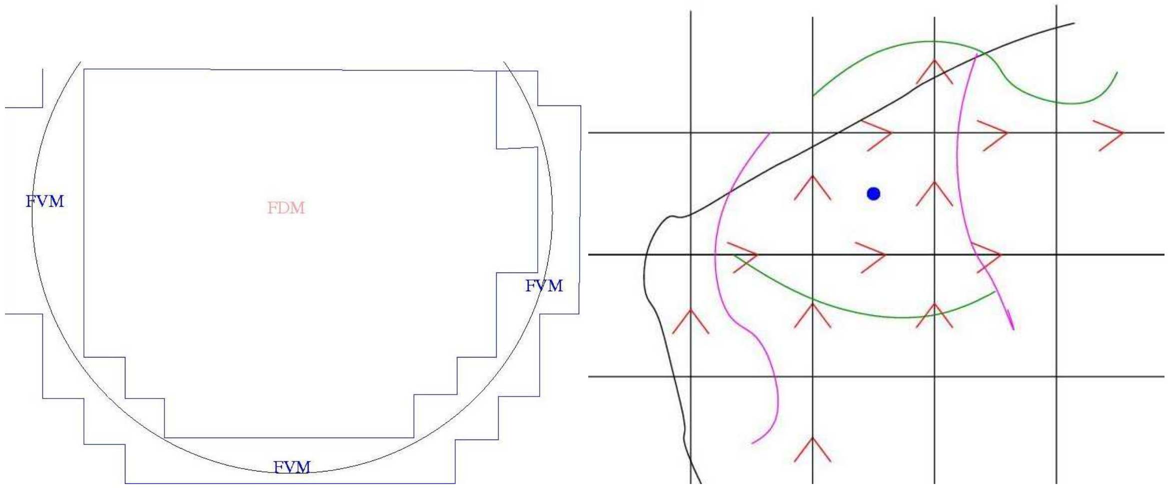

Figure 5.6: Left: fv-fd coupling; right: integrate E field to calculate curl H

volume approximation, the average value, which is defined as integral value over area, is approximated by an center value with a 2nd order error term. Therefore in the 2nd order EBM, $H_{i,j,k}$ represents an average value of the extended area instead of the point value.

It is natural to consider the 4th order mapping between the point value and the average value to extend the 2nd order EBM to 4th order EBM. The other ideas of 2nd order EBM will be kept in 4th order EBM. The position of average value for magnetic field in cut cell is still in the center of extended cell. The position of point value for electric field is still in the center of cell edge. Center scheme for spatial discretization is adopted but we need to use 4th order schemes.

The 2nd order EBM for the interior cells is the same as the general FDTD method. This gives a concise mathematical formula, but for the 4th order EBM, we lose such advantage. We need to deal with interior cells by 4th order FDTD and deal with cut cells by 4th order EBM separately.

3 steps for cut cell EBM:

(1) Update the point value E^{n+1} from E^n and $\hat{H}^n$ by using the 4th order spatial

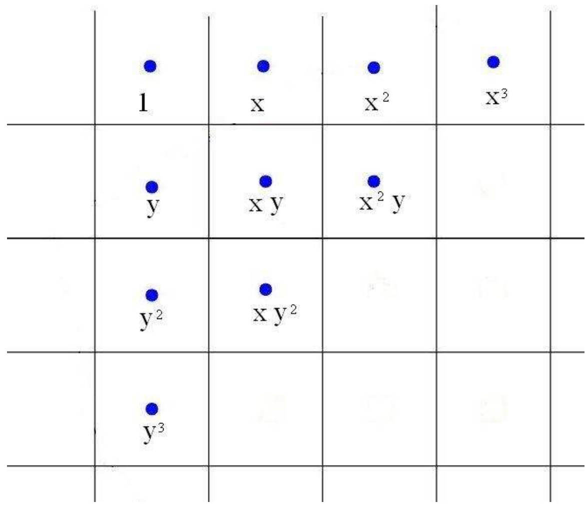

Figure 5.7: Full-rank 10-point stencil

discretization of derivatives. If the point is near the boundary, 3rd order one-side derivatives will be calculated to avoid using outside information.
(2) Update the average value $\hat{H}^{n+1}$ by integration for E^{n+1} along the cut cell boundaries and $\hat{H}^{n}$ in the center of the extended cell. We may use a cubic polynomial to fit E field and integrate the cubic polynomial.
(3) Mapping between H^{n+1} and $\hat{H}^{n+1}$ can be obtained by a 2D cubic polynomial fit to the magnetic field. 2D cubic polynomial contains 10 coefficients, so at least 10 points are required to calculate the coefficients. There are 2 choices. One is to use exact 10-point stencil; the other way is to using more than 10 points and then solve least square problem.

This discretization cannot be combined with an explicit time scheme, otherwise it will not be stable. Implicit method may bring stability, but implicit method is more time consuming.

The mapping from $\hat{H}$ to H is not easy to obtain. The computation requires reverse matrix computing for a big size matrix which contain the geometric information for all cut cells in whole computational domain. EM structures usually do not change shape during computing process. In this case, we just need to calculate the reverse matrix once, at the first time step, and can use it directly in all other computing steps.

Chapter 6

Conclusions

We performed simulation of hydrodynamic processes in the plasma jet induced magnetized target fusion.

(1) Deuterium jet propagation is simulated with MUSCL scheme and the profile of density, pressure and velocity field are obtained. A new jet radius increasing prediction model is compared with this numerical simulation. Since the jet moving in high vacuum is adiabatically cools down and gains the radial componetn of velocity, the Mach number increasing and temperature decreasing are observed. With weight of density factor, the Mach number of jets increases from 60 to around 110 in a 6-meter chamber.

(2) The process of the jet merger and the formation of liner is simulated with different chamber radius, 3 meter and 6 meter, and different merging radius, 50 cm and 1 meter. Simulations were performed on New York Blue using 4096 processors. Simulations confirmed a possibility to form sufficiently uniform liner. The Mach number decreasing for liner merging is studied for different mesh and good convergence result is shown. The different liner structures of density and pressure are analyzed. The bigger merging radius is, the more jets we need. As a results, the deviation is bigger, however the relative deviation is smaller, so a more uniform liner will be obtained.

(3) Spherically symmetric simulations of the implosion of plasma liners and compression of plasma targets have also been performed using the method of front tracking. The cases of single deuterium and xenon liners and double layer deuterium - xenon liners compressing various deuterium-tritium targets have been investigated, optimized for maximum fusion energy gains, and compared with theoretical predictions and scaling laws of [P. Parks, On the efficacy of imploding plasma liners for magnetized fusion target compression, Phys. Plasmas **15**, 062506 (2008)]. In agreement with the theory, the fusion gain was significantly below unity for deuterium - tritium targets compressed by Mach 60 deuterium liners. In the most optimal setup for a given chamber size that contained a target with the initial radius of 20 cm compressed by 10 cm thick, Mach 60 xenon liner, the target ignition and fusion energy gain of 10 was achieved. Simulations also showed that composite deuterium - xenon liners reduce the energy gain due to lower target compression rates. The effect of heating of targets by alpha particles on the fusion energy gain has also been investigated. The study of the dependence of the ram pressure amplification on radial compressibility showed a good agreement with the theory. The study concludes that a liner with higher Mach number and lower adiabatic index gamma (the radio of specific heats) will generate higher ram pressure amplification and higher fusion energy gain.

We also implemented 3 dimensional, second order embedded boundary method for complex geometries and forth order symplectic method for the Maxwell equations. Stability and error analysis are proved in both numerical experiments and in theory. Until now, our PJMIF simulations consider only hydrodynamic process. In future MHD process will be considered in the liner target interaction simulation. The second order embedded boundary method for Maxwell equations will be the main component of an electromagnetic particle-in-cell code for the simulation of plasma guns.

Bibliography

[1] H.S. Bosch and G.M. Hale. Improved formulas for fusion cross-sections and thermal reactivities. *Nucl. Fusion*, 32:611, 1992.

[2] J. T. Cassibry, R. J. Cortez, S. C. Hsu, and F. D. Witherspoon. Estimates of confinement time and energy gain for plasma liner driven magnetoinertial fusion using an analytic self-similar converging shock model. *Phys. Plasmas*, 16:112707, 2009.

[3] David K. Cheng. *Field and Wave Electromagnetics*. 2nd edition, 1989.

[4] Supriyo Dey and Raj Mittra. A locally conformal finite-difference time-domain (fdtd) algorithm for modeling three-dimensional perfectly conducting objects. *IEEE MICROWAVE AND GUIDED WAVE LETTERS*, 7:273, 1997.

[5] J. Du, B. Fix, J. Glimm, X. Jia, X. Li, Y. Li, and L. Wu. A simple package for front tracking. *J. Comp. Phys*, 213:613, 2006.

[6] Qiang Du, Vance Faber, and Max Gunzburger. Centroidal voronoi tessellations: Applications and algorithms. *SIAM Review*, 41:637–676, 1999.

[7] J. Glimm, M.J. Graham, J.W. Grove, X.L Li, T.M. Smith, D. Tan, F. Tangerman, and Q. Zhang. Front tracking in two and three dimensions. *Comput. Math. Appl.*, 35:1–11, 1998.

[8] J. Glimm, J.W. Grove, X.L Li, and D. Tan. Robus computational algorithms for dynamic interface tracking in three dimensions. *SIAM J. Sci Comp.*, 21:2240–2256, 2000.

[9] Johansen H and Colella P. A cartesian grid embedding boundary method for poisson's equation on irregular domains. *Journal of Computing Physics*, 147:60–85, 1998.

[10] A. Hasegawa, K. Nishihara, H. Daido, M. Fujita, R. Ishizaki, F. F. Miki, K. Mima, M. Murakami, S. Nakai, K. Terai, and C. Yamanaka. Magnetically insulated and inertially confined fusion – micf. *Nucl. Fusion*, 28:369, 1988.

[11] Roger W. Hockney and James W. Eastwood. *Computer Simulation Using Particles*. CRC Press, 1988.

[12] Scott Hsu, F.Douglas Witherspoon, Jason Cassibry, Mark Gilmore, and Richard Siemon. Formation of imploding plasma liners for hedp and mif applications.

[13] R. C. Kirkpatrick, I. R. Lindemuth, and M. S. Ward. An overview of magnetized target fusion. *Fusion Technol*, 27:201, 1995.

[14] Charles E. Knapp. *An implicit smooth particle hydronamic code*. PhD thesis, Los Alamos national laboratory, 2000.

[15] Tianshi Lu. Stablity condition for maxwell equation. 2009.

[16] McCorquodale P, Colella P, and Johansen H. A cartesian grid embedding boundary method for the heat equation on irregular domains. *Journal of Computing Physics*, 173:620–635, 2001.

[17] Schwartz P, Barad M, colella P, and Ligocki T. A cartesian grid embedding boundary method for the heat equation and poisson's equation in three dimensions. *Journal of Computing Physics*, 211:531–550, 2006.

[18] P.B. Parks. On the efficacy of imploding plasma liners for magnetized fusion target compression. *Physics of plasmas*, 15:062506, 2008.

[19] D.D. Ryutov, M.S. Derzon, and M.K. Matzen. The physics of fast z pinches. *Rev. Mod. Phys*, 72:167, 2000.

[20] R. Samulyak, J. Du, J. Glimm, and Z. Xu. A numerical algorithm for mhd of free surface flows at low magnetic reynolds numbers. *J. Comp. Phys*, 226:1532, 2007.

[21] Roman Samulyak, Jian Du, James Glimm, and Zhiliang Xu. A numerical algorithm for mhd of free surface flows at low magnetic reynolds numbers. *Journal of Computational Physics*, 226(2):1532–1549, 2007.

[22] Roman Samulyak, Paul Parks, and Lingling Wu. Spherically symmetric study of plasma liner implosion for magnetized target fusion. 2009.

[23] J.A. Sethian. Level set method. *Cambridge University Press*, 1996.

[24] A. Sherwood. Megagauss physics and technology. *Second International Conference on Megagauss Magnetic Field Generation and Related Topics*, Washington, D.C:375, 1980.

[25] Y. C. Francis Thio and Ronald. C. Kirkpatrick. Magnetized target fusion driven by plasma liners. *Annual Meeting of the American Nuclear Society*, Hollywood:FL, 2002.

[26] Y.C.F. Thio, E. Panarella, R.C. Kirkpatrick, C.E. Knapp, F.Wysocki, P. Parks., and G. Schmidt. Magnetized target fusion in a spheroidal geometry with standoff drivers. *Current trend in international fusion research*, 1999.

[27] Shuqiang Wang, Roman Samulyak, and Tongfei Guo. An embedded boundary method for elliptic and parabolic problems with interfaces and application to multi-material systems with phase transitions. *Acta Mathematica Scientia*, 30B(2):499–521, 2010.

[28] Kane Yee. Numerical solution of initial boundary value problems involving maxwell's equations in isotropic media. *Antennas and Propagation*, 14:302–307, 1966.

[29] A. Yefet and E. Turkel. Fourth order compact implicit method for the maxwell equations with discontinuous coefficients. *Applied Numerical Mathematics*, 33:125–134, 2000.

[30] Kaoru Yoshida, Michael P.Strathmann, Carol A.Mayeda, Christopher H.Martin, and Michael J.Palazzolo. A simple and efficient method for constructing high resolution physical maps. *Nucleic Acids Research*, 21:553 –3562, 1993.